nature portfolio

https://doi.org/10.1038/s41586-022-05199-7

Supplementary information

A universal coupling mechanism of respiratory complex I

In the format provided by the authors and unedited

Supplementary Information contents:

Supplementary Discussion.

Supplementary Figures S1-S13 – cryo-EM data processing overview. Processing procedure, 2D and 3D classes, FSC plots, angular distribution plots and local resolution maps are shown.

Supplementary Tables:

Table S1, Model overview.

Tables S2-S6, Data processing and refinement statistics, *E. coli* CI.

Table S7, Data processing and refinement statistics, ovine CI.

Table S8, Mutations in the *E. coli* complex I and their structural context.

Video S1.

Density overview of cryo-EM maps from the LMNG_Turnover_pH6 dataset.

Video S2.

Global conformational changes occurring upon *Ec*CI closing. Pale surface shows Q cavity. Disordered NuoA and NuoH loops in the open state were modelled for representation purposes.

Video S3.

Conformational changes of the key Q cavity loops upon *Ec*CI closing. Pale surface shows Q cavity. Disordered NuoA and NuoH loops in the open state were modelled for representation purposes.

Supplementary Discussion

1. The role of bound lipids

Earlier studies have shown that lipids are essential for *Ec*CI activity and stability[26]. We observe about 16 lipid molecules along the MA (ED Fig. 4a). Most lipids stabilise the interfaces between subunits, in positions consistent with recent mitochondrial CI structures[3,7,20]. Importantly, the open/closed states classes show more bound lipids than the resting state, in particular around the NuoI amphipathic helix H1, which is disordered in the resting state (ED Fig. 2d). The lipids near $_{I}$H1 probably play a critical role in promoting $_{I}$H1 binding to NuoH and NuoCD subunits, securing the PA/MA interface. In high DDM the detergent likely delipidates this area, preventing the closing of the interface and resulting in the observation of the resting state only. The open/closed states are characterised by the ordered $_{I}$H1 and also by the formation of four salt bridges linking the PA and MA subunits (ED Fig. 2d). Consistently, we observe markedly larger hydrophobic detergent/lipid belt around the MA in DDM/LMNG and LMNG datasets compared to DDM datasets (ED Fig. 4b). The dispersion of the PA-MA angle is much lower in open/closed state classes as compared to the resting state, suggesting that they are more "rigid" and better defined than the uncoupled resting conformation. The fact that the resting structure is the same in all datasets, including LMNG, and that in resting state $_{H}$TM5-6 loop has a defined "up" conformation, different from "down" in closed state, suggests that the resting state is not an artefact of detergent exposure but is a genuine conformation of *Ec*CI. Since it does not disappear under turnover, it is not clear whether the resting state can be defined just as the state waiting to recover full activity. Perhaps, as an alternative or in addition, some population of the protein can enter such a state periodically even during turnover as a way to "rest" for a few cycles.

2. Peripheral Arm structure

High resolution allowed us to improve the previous crystal structure of the MA [9], while the structures of the NuoH and the PA are new (ED Fig. 2), solved independently before recently published structures[21,57]. The general structure resembles the known core complex I architecture, with a few key differences. *Ec*CI has the largest NuoG subunit among known CI structures, with a long (~100 residues) insertion loop with a unique structure (ED Fig. 2a). The loop stabilizes the complex by increasing the interaction surface area mainly with the NuoCD subunit, effectively replacing such accessory subunits as the Nqo16 from *Tt*CI

or the mammalian 18 kDa subunit. Calcium is essential for *Ec*CI activity and stability[26] and NuoG subunit contains a Ca^{2+} ion bound at the site unique for *E. coli*, coordinated by acidic residues from the insertion loop (ED Figs. 1h and 2a). NuoC and D subunits are fused in *E. coli* by a species-specific loop-helix-loop ($_{CD}$LHL) element, which interacts with NuoG, B and A subunits, stabilising the interface region (Fig. 2a and ED Fig. 2a). Additional inter-subunit interactions are provided by the *E. coli*-specific C-terminal extensions of about 20 to 40 residues in subunits NuoB, I, and F, stabilising the "back" of the PA (ED Fig. 2b). It is likely that all these extensions are necessary to maintain the stability of the minimal version of complex I, as their sequences are conserved in Enterobacteria. The enzymes lacking such extensions instead contain additional subunits (*T. thermophilus*[4], *Paracoccus denitrificans*[58] and mitochondrial).

In contrast to other species, in *Ec*CI the N1a cluster has an unusually high redox potential (~ -235 mV in *E. coli vs* < - 400 mV in *P. denitrificans* or bovine) and can be reduced by NADH [59,60]. The structure reveals that $_{E}$N142 forms a strong hydrogen bond to the N1a S atom (ED Fig. 1k). This polar residue is unique to *E. coli*, as it is replaced by a hydrophobic Met or Val in other species[61]. The potential of FeS cluster can be increased by the polar interactions, including solvent waters[62]. One of the two waters resolved near the cluster N1a in *E. coli* forms a hydrogen bond to the Sγ atom of $_{E}$C97 (ED Fig. 1k). This water is absent in ovine enzyme, while the second water, bonded to $_{E}$C133, is present (PDB 6zk9). Therefore, the higher N1a redox potential in *E. coli* can be attributed to the unique $_{E}$N142, consistent with the effects of mutations of this residue[53,61], as well as to the additional water molecule.

Most other clusters in the redox chain lack waters in their immediate environment, both in *E. coli* and in ovine, and are mostly equipotential at about -250/-300 mV [54,63]. The terminal cluster N2, which has the highest potential in the chain (~ -200 mV in *E. coli* [63] and -140 mV in bovine[64]), is a clear exception as it has two waters forming hydrogen bonds to the cluster. The waters' position is conserved between *E. coli* and ovine enzymes (ED Fig. 1j). Additionally, this cluster interacts with the conserved NuoCD residues R254, R274 and H359. This highly polar environment explains the high potential of the cluster. Overall, up to 860 waters are observed within the highly hydrated PA, and some waters closer to the core of the protein are conserved with the ovine enzyme, including the two waters situated roughly between the N3 and N4 (ED Fig. 2c) but located too far from the clusters for any direct interactions.

Complex I is a major source of ROS with the fully reduced FMN being the main producer[65]. In the bovine enzyme, FMN predominantly donates an electron to O_2 forming superoxide, which is detoxified to H_2O_2 by superoxide dismutase[66]. In contrast, *Ec*CI forms H_2O_2 directly, which is not due to the high N1a potential[61]. We compared the NADH-binding sites of *Tt*, *Aquifex aeolicus* (*Aa)*, *Yarrowia lipolytica (Yl)* and mammalian NuoF structures with *Ec*CI. About 8 Å from FMN we identified an arginine residue ($_F$R320), which is not present in other structures (ED Fig. 2g), being replaced by Gly in the mitochondrial and by Met in the *Tt* enzymes. It is thus possible that the extra positive charge on $_F$R320 retains the nascent superoxide long enough for the spontaneous degradation into hydrogen peroxide to happen. Additionally, when NADH is bound, this arginine forms a tight hydrogen bond to the ribose moiety of NADH. This possibly changes the kinetics of NADH/NAD^+ binding/release and, as a consequence, ROS production. Mutagenesis on R320 would be necessary to verify these hypotheses.

Recently, from the analysis of structures of the *Aa*NuoFE subcomplex, it was suggested that the peptide bond between E95 and S96 ($_F$E93 and $_F$M94 in *Ec*CI) flips away from FMN in the reduced state and towards FMN in oxidized, as a mechanism to reduce ROS production[52]. This contradicts our high-resolution structures - the peptide is clearly always oriented away from FMN (ED Fig. 2ef), similarly to *Oa*CI [3]. The difference with *Aa* is likely due to the different properties of the protein and the FeS clusters in a two-subunit subcomplex as compared to the intact enzyme[52,67].

When the *E. coli*[53] or bovine[68] enzyme is reduced by NADH in the absence of electron acceptors (DQ or FeCy), FMN reversibly dissociates from the complex, as a possible mechanism for the prevention of ROS production[53]. The dissociation is prevented at high protein concentrations when protein-bound FMN concentration exceeds the K_d for FMN dissociation[53]. Our DDM datasets were obtained with high *Ec*CI concentration on a grid, 8-10 mg/ml, as compared to ~0.2 mg/ml in DDM/LMNG, due to the use of the carbon support in the latter case. Consistently, in the structure of the reduced enzyme in DDM (DDM_NADH) we did not observe FMN dissociation and saw clear NADH density alongside FMN (ED Fig. 3a). However, in DDM/LMNG_PieA+NADH dataset substantial parts of NuoF and NuoE subunits (including FMN) were disordered and had a weak density (ED Fig. 3c). In the DDM/LMNG_NADH+FMN dataset, external FMN was added, which according to the experimental data recovers the electron transfer activity[53]. Indeed, we observed stronger FMN density, although NuoF and E subunits were still substantially

disordered (ED Fig. 3d). These data unequivocally confirm our original proposal that FMN dissociates under these conditions, in contrast to alternative explanations[69].

Importantly, in the turnover dataset, FMN, NADH, NuoF and NuoE all have strong densities (ED Fig. 3b), confirming that the constant electron transfer from NADH to DQ was happening at the time of flash-freezing (otherwise NuoF and NuoE would be disordered and FMN would dissociate as in ED Fig. 3c [53]).

3. Proton translocation pathways

Proton transfer pathways (Fig. 3a) were identified by connecting Grotthuss-competent residues (Lys, Glu, Asp, His, Tyr, Thr, Ser[70]) and experimentally observed waters within hydrogen bonding distances (with ~4 Å slack).

NuoL ALS is markedly different as it possesses a highly hydrated path, completely absent in NuoN/M, connecting the cytoplasm to periplasm via conserved K305, K342, H254, H334 and H338 (located around TM8), exiting to the periplasm near LysTM12 (K399) via D400 and the surrounding polar residues and waters. This highly polar exit area around $_{L}$D400 is unique to NuoL, and consistently, NuoL shows high sequence conservation from the matrix to the periplasmic surface, while NuoN/M are mostly conserved only around the central axis[3]. In NuoN/M, areas around Lys/GluTM12 (and the entire periplasmic side) are devoid of waters in all of *Ec*CI structures and are blocked from the periplasm by large hydrophobic residues. The same is true for the analogous area in the E-channel. Since we did not observe any conformational changes in the ALS under any conditions including turnover, a temporary formation of exit pathways in NuoN/M and E-channel is unlikely. These observations suggest that proposal[3] on the NuoL-only proton exit holds true for complex I in all species, from bacterial to mammalian.

Following the proton pathways further along the central axis, it appears that in *Ec*CI (as in *Y. lipolytica*[20]) there is no connection from the $_{L}$TM8 area to LysTM7, in contrast to mammalian[3], NDH and plant mitochondrial enzyme. This is because $_{L}$H254, which replaces LysTM8 in NuoL, in these species is rotated on the TM8 π-bulge to establish a connection towards LysTM7 (ED Fig. 7d). This histidine remains in its stable position in all states of *Ec*CI and *Oa*CI, but in a related MRP antiporter it was resolved in a double conformation[71], suggesting that its flexibility may be functional in some cases. Such a switch would direct protons incoming from the matrix into NuoL either towards the rest of the central axis or towards $_{L}$LysTM12, helping to distribute incoming protons over the entire central axis.

Additionally, it may help to prevent wasteful back-flow of protons from $_{L}$LysTM12 towards cytoplasm.

Further on, a large number of waters help to establish a strong inter-subunit connection: $_{L}$LysTM7(K229)-$_{L}$GluTM5(E144)-$_{M}$GluTM12(E407)-$_{M}$H322-$_{M}$H348-$_{M}$H248-$_{M}$K312 to the cytoplasm. This path is branching off towards $_{M}$LysTM7(K234) via $_{M}$LysTM8 (K265). This key lysine sits on a short inner loop (i.e. heavily unwound helix) part of TM8. In our earlier otherwise very similar crystal structure of the membrane domain (PDB 3RKO[9]), this loop adopted a very different, less unwound structure with the cytosolic half of TM8 rotated by two residues (ED Fig. 7e). The TM8 density is well defined and its register is the same in all our cryo-EM structures. This suggests that this flexible helix adopts a strained unwound conformation (necessary for function) in the intact complex and it rewinds into a more helical-like state under low pH crystallisation conditions, which separate MA from PA[9]. We did not observe a 3RKO-like conformation of this helix in cryo-EM data under any redox conditions. Moreover, in the cryo-EM conformation, the register of the helix is much more consistent with other CI structures (ED Fig. 7e). This suggests that, although apparently attractive, the idea of $_{M}$TM8 helix rotating during the catalytic cycle to a similar extent as $_{J}$TM3 is unlikely. However, the loop around K265 did adopt two different conformations in different cryo-EM structures: in the first, "linked" conformation (green in ED Fig. 7e), K265 sits between H348 and K234 (LysTM7). In the second conformation (grey in ED Fig. 7e), K265 is flipped away, and L264 partially blocks the path towards LysTM7. Thus, the link along the hydrophilic axis from GluTM12 to LysTM7 in NuoM would be optimal only with the "linked" conformation of TM8 loop, although the L264 block in "flipped" conformation can probably be bypassed via H248. Nevertheless, the strained but flexible conformation of TM8 loop suggests that temporary on/off switch in the axial link in NuoM is likely to be important for the optimal function. There is, however, no clear pattern under which conditions a particular conformation is observed in our structures, suggesting that the switch is not directly linked to the redox state but perhaps reacts to a particular set of charges on key residues. In the mammalian enzyme this area is less strained, more helical (a classical π-bulge) and we did not observe any change in conformation under any redox conditions[3], suggesting that K265 flip is either specific to some species like *E. coli*, or that it is too transient to be observed in mammalian enzyme. Overall, such flexibility around $_{M}$K265 probably helps with proton re-distribution along the central axis and prevents back-flows similarly to $_{L}$H254.

The link to the cytoplasm ($_{M}$H248-$_{M}$K312) appears to represent a characteristic ALS motif: in NuoM these residues are linked by $_{M}$D258 from TM8, while in NuoL similarly arranged $_{L}$H254 and $_{L}$K305 are connected by $_{L}$S250. In both cases, the histidine sits on a broken helix: TM8 in NuoL and TM7 in NuoM, with side-chain placed into a similar position. $_{M}$D258 is conserved only as a polar residue, being replaced by a serine in mammalian enzyme. Importantly, this H-Polar-K motif is absent in NuoN, where only the surface-exposed lysine is conserved and the histidine is replaced by an inwards-facing tyrosine.

Moving on along the central axis, we observe again abundantly hydrated inter-subunit links via $_{M}$LysTM7(K234)-$_{M}$GluTM5(E144)-$_{N}$LysTM12(K395)-$_{N}$H305-$_{N}$Y333-$_{N}$LysTM8(K247)-$_{N}$LysTM7(K217)-$_{N}$GluTM5(E133). Due to the absence of the H-Polar-K motif, links to the cytoplasm in NuoN are absent, as noted also for *Oa*CI[3]. Furthermore, in contrast to NuoM/L, the area around $_{N}$LysTM8 is almost helical with only a minor π-bulge (and it is of similar appearance in other species), suggesting much less flexibility. Therefore, subunit NuoN appears to be specialised for inter-subunit axial transfer of protons with no evidence for input from cytosol.

The central axis ends with the E-channel and the $_{CD}$D329/H228 pair, a likely source of two substrate protons for quinone[3,4]. Considering that in *Y. lipolytica* Y144F (corresponding to *Ec*CI $_{CD}$Y277) mutant was fully active with Q1/Q2 (but not with DQ or native Q9)[72], the tyrosine may not donate protons but rather help to coordinate Q via H-bond to carbonyl (less important with flexible Q1/Q2), as we observe (ED Fig. 7b).

4. Mutagenesis studies

The effects of a large number of site-specific mutations studied in *Ec*CI are highly consistent with our mechanism (Fig. 3a and Supplementary Table S8). Mutations to any of the key charged residues along the central axis strongly diminish both the oxidoreduction activity and proton pumping, as expected when the main proton transfer path along central axis is disrupted. The inhibition of activity is almost complete even with mutations in the distal subunit NuoL, which would be difficult to explain on the basis of purely conformational coupling.

To clarify the role of the key charged residues, we introduced additional chromosomal complex I mutations in *E. coli*. Mutations to $_{N}$E133, $_{N}$K217 and $_{M}$E144 strengthen earlier observations[73] that at the *TM7/TM5* site the effects are milder in NuoN than in NuoM/L (ED

Fig. 8). This is likely due to the high concentration of charged residues in this area in NuoN, including NuoK glutamates. Therefore, the effects of any single mutation can be compensated and bypassed by neighbouring residues. Indeed, double $_{N}$E133A/$_{K}$E72A mutation leads to the strong inhibition of activity[73]. However, the *TM12* residue K395 is as essential in NuoN (ED Fig. 8) as in NuoL, confirming a central and irreplaceable role of the *TM12* sites.

One *TM12* residue of particular interest is $_{M}$E407, as it is the only one in ALS where the key *TM12* residue is a glutamate. In the homologous MrpD subunit in the ancestral MRP complex this residue is a lysine, so it is not clear how essential is a replacement to glutamate, conserved in complex I. Previously we discussed that due to this mutation NuoM subunit might work in antiphase to NuoN/L[3]. A conservative $_{M}$E407D mutation preserved both the oxidoreductase and the proton pumping activities, while $_{M}$E407Q and $_{M}$E407A[73] mutations were strongly inhibitory (ED Fig. 8). Importantly, $_{M}$E407K mutation preserved both activities – this indicates that having glutamate as a key $_{M}$TM12 residue is not essential and lysine can also perform this role. This emphasises the similarity of the general mechanism between the MRP antiporters and modern complex I-like enzymes, as well as argues against the "antiphase" function of NuoM. Although activity was preserved in $_{M}$E407K, the cell growth was delayed compared to WT (ED Fig. 8a), suggesting that although glutamate in this position is not essential for complex I function, the rest of the protein likely adapted for this change, e.g. by the addition of $_{L}$R175 at NuoL/M interface. Nevertheless, the viability of $_{M}$E407K suggests that all three antiporters function in a similar manner, consistent with our mechanism.

A controversy has arisen recently due to proposals, based on cross-linking and labelling experiments[31,74], that quinones can enter the cavity not through the main entry but through a site analogous to our W site for waters. Although these proposals contradict numerous structures with quinones bound at different points along the main Q channel (reported here and in refs.[3,8,75,76]), we decided to verify the uniqueness of the main access path with mutations. $_{H}$M64 and $_{H}$M67 surround the entrance to the cavity, ensuring, within the ring of hydrophobic residues, the tight fit around the tail of quinone bound inside (ED Fig. 5d). Mutations of either residue to alanine strongly diminished both DQ and proton pumping activities (ED Fig. 9), suggesting that the tight fit around the tail is important for optimal quinone passage into the cavity. $_{H}$M64T (to mimic the common human LHON mutation A52T) and $_{H}$M67W (to block the entry with bulky residue) mutations completely abolished all activities, unequivocally confirming that the main entry point is the only one used by

quinones (and not a W site). WT *Ec*CI is insensitive to rotenone, a bulky specific inhibitor of mammalian enzyme, which, despite its size, binds within the main cavity in *Oa*CI[3]. Interestingly, *Ec*CI $_{H}$M67A mutant could be inhibited by rotenone (ED Fig. 9d), suggesting that the inhibitor is able to enter the cavity through a widened main entry point. Thus, these mutations confirm that quinone and hydrophobic inhibitors enter the cavity via the main entry point, while the W site is used for water access, as we propose. On the other hand, hydrophilic cross-linkers may also enter via W site, explaining labelling results[31]. Overall, most mutations were notably more detrimental for reactions with the native quinone (dNADH:O_2 activity) than with the short-tailed DQ (ED Figs. 8-9), consistent with the proposed role of quinone tail (blocking the cavity) for optimal coupling.

5. A/D transition of mammalian complex I and closed/open states

Mammalian CI is unique since apo-enzyme (i.e. in the absence of turnover or any substrates) can exist in the mixture of closed, open and also deactive states. This is likely due to the high-energy barrier for transitions between these states in the absence of substrates. The barrier is known to be very high for A/D transition and is likely lower but still significant for closed/open transition, since both closed and open states can be observed in apo-enzyme. This feature is possibly associated with the optimization of mammalian enzyme to avoid any slips or leaks. The ratio between the states depends on the species and purification history – the longer/more extensive the purification is, the more open state is observed. However, when kept at 4^{o}C during standard purification the enzyme does not enter the deactive state, as evidenced by the absence of any lag in reaching full activity after initiating turnover[3]. Only after prolonged (up to 1 hour) heating to ~37ºC without substrates the enzyme converts to 100% deactive state, which is characterized biochemically by the lag in developing activity and structurally by the complete relocation of $_{J}$TM4[3].

The apo closed state can be termed rather closed-like state, since there is no quinone bound in this case, unlike in the true closed state under turnover. We observed ~10% closed-like state with the purified *Oa*CI[3], while our milder procedure to produce respiratory supercomplexes resulted in about 30% closed-like[38], and mouse enzyme, which can be isolated quickly, shows mostly closed-like state[7]. The proportion of closed-like state may depend in part on the amount of specific native lipids retained during purification. Under CI turnover it could be expected that both true closed and open states would be observed, even if one of them heavily dominates, as was the case for the open state of *Oa*CI[3]. Therefore, if

mouse enzyme could be purified in almost 100% closed state, it would be expected that some proportion of open state would appear under turnover.

Overall, the tendency of mammalian CI to slowly relax into open state over prolonged purification may be misleading into thinking that open and deactive states are identical, since they have some of the similar features, including disorder of Q loops and the related sensitivity to NEM. However, it is clear that deactive state is distinct and separated by a large energy barrier (due to ⱼTM4 relocation) from the open state in the overall spectrum of closed-open-deactive states of mammalian enzyme. Even though the closed-like-to-open ratio can be quite variable for a particular enzyme depending on purification procedure, the catalytic activity remains the same for the identical assay conditions.

On the other hand, as noted in the main text, all non-mammalian species studied so far show only open-like states. They also do not show a pronounced A/D transition (including *Y. lipolytica,* where A/D energy barrier is small[20]). Therefore in these species in the absence of turnover the enzyme quickly relaxes from the mixture of closed/open states into lower energy open state even during mild purification at low temperature. Only upon turnover both closed and open states would be then observed, exactly as we see with *E. coli*. In the recently reported structure of $CICIII_2$ from the ciliate *Tetrahymena thermophila* complex I appears to be only in the closed-like state, although this enzyme is quite divergent from classical CI [77]. Authors propose that this may be the only active state of this complex. However, data under turnover conditions, when the open state may be observed as well, were not collected in this case, so the essential data is missing.

In our current study the ovine enzyme was subject to pre-turnover in membranes, which increased the proportion of closed state at pH 7.4 from ~10% to ~31%. We note that this is not a pre-activation procedure *per se*, since according to biochemical assays there was no deactive enzyme within the preparation[3]. Rather, the equilibrium in the closed/open state energy profile shifted more towards closed-like state, possibly because more of native lipids (those relevant to promote closed-like state) could be retained after such treatment and subsequent purification. An alternative way to retain native lipids could be the study of CI within supercomplexes, giving 30% (ovine[38]) to 60% (porcine[19]) closed-like state.

The W site explains the experimental observations with *Y. lipolytica* mutant in which the $_{ND3}$C40 ($_{A}$S52 homolog) was cross-linked to $_{PSST}$Q133C ($_{B}$R112 in *E. coli*) to fix the ND3/NuoA loop in place[78]. In the WT structure[75] these two residues are as much as 11 Å apart, therefore the cross-linked NuoA loop would be likely distorted and fixed in the position which leaves the W site permanently open (as also noted recently[79]). According to

our mechanism, this will allow quinone protonation by external waters in the closed state and thus completely un-couple proton pumping from oxidoreduction, exactly as observed[75].

6. Turnover conditions

Verified turnover conditions are in principle challenging to achieve for complex I, because the substrates can be used up within seconds due to high protein concentration in the sample on the cryo-EM grid. This is especially the case for quinone due to its limited solubility in aqueous solutions. Other researchers tried to overcome this problem by introducing quinone regeneration system with ubiquinol oxidase[20]. In our hands, however, the addition of such oxidase introduced too much background signal in cryo-EM images. Therefore, for *Ec*CI we used grids with continuous carbon support, which allowed us to dramatically lower CI concentration (from ~5-10 mg/ml to ~0.2 mg/ml). This ensured that available DQ was not used up within time frame from NADH addition to snap-freezing of the sample (Methods). The full turnover conditions were verified by at least three independent lines of evidence: 1) activity assays following NADH absorbance in the sample prepared under exact same conditions as for cryo-EM, using Nanodrop spectrophotometer; 2) the presence of strong cryo-EM density from FMN, NADH, NuoF and NuoE in turnover data, which is otherwise absent in NADH-reduced *Ec*CI in the absence of turnover (ED Fig. 3); and 3) the closed state, with quinone bound in Q_d site, appears only under turnover (in three independent datasets).

Previously, instead of using diluted protein on carbon-coated grids as for *Ec*CI, we ensured full turnover conditions for mammalian CI by chilling the sample to reduce the activity. The procedure was only briefly described due to the lack of space[3]. In their online comment[80], V. Kaila and J. Hirst challenged the existence of turnover on the basis of flawed assumptions. We clarify the points raised and provide more details here. First, the NADH:DQ activity of the *Oa*CI purified in LMNG as used in our study was nearly identical to that in the native membranes (~ 5-6 U/mg CI purified vs ~ 7 U/mg CI in the membranes[81]), so it is not "damaged" (as alleged) in any way. Second, as we have shown[3], the deactive state is structurally very much distinct from the open state and it was present only in a specifically deactivated preparation, in contrast to the assumptions in the comment, which ignored these clear findings. Third, it was noted that the proportion of closed/open states of *Oa*CI did not change under turnover. It is likely that for *Oa*CI the energy profiles of closed-like/open apo states and closed/open turnover states are similar (perhaps even coincidentally) and so the proportion did not change in this case. Importantly, the

appearance of closed *Ec*CI state only under turnover in the current study firmly establishes that closed/open states are indeed catalytic intermediates. Fourth, for the turnover *Oa*CI sample, as for others[3], the mixing with NADH was performed on ice, followed by deposition on the grid kept at 4°C. Therefore during the entire ~20 s procedure the sample was at 4°C. At this temperature the activity of *Oa*CI drops to ~0.2 U/mg protein (no lipids in the buffer) or ~0.5 U/mg protein (with lipids) but remains fully sensitive to rotenone. Thus, apart from slowing down the reaction, these conditions should not influence its mechanics. In the cryo-EM sample (no lipids in the buffer) the endogenous lipids will be partially concentrated with the protein, so the activity is likely to be between 0.2 and 0.5 U/mg protein. Therefore the amount of substrate to be used within 20 s would be ~10-25% of the initial 2 mM NADH and DQ. The turnover conditions were further confirmed using Nanodrop in the same way as for *Ec*CI. Therefore there is no doubt that *Oa*CI turnover dataset was collected under turnover conditions, as is also obvious from structural features.

7. The "open-ready" state of *Ec*CI

The "open-ready" state differs from "open" mainly by conformations of $_{H}$TM5-6 and NuoCD loops. The $_{H}$TM5-6 loop, disordered in open state, adopts ordered conformation differing from closed state by the reorganisation bringing invariant $_{H}$E220 close to $_{CD}$H224 (Fig. 2c). This interaction compensates for $_{CD}$H224 charge and thus allows two invariant essential histidines from NuoCD loop (H224 and H228) to form a strong interaction characterised by solid connecting cryo-EM density (ED Fig. 1c). This interaction stabilises the extended NuoCD loop, preventing Q_d binding. A similar conformation is observed in NADH-reduced open states, perhaps stabilised by the negative charge on N2 cluster. Otherwise, $_{CD}$H224 and $_{CD}$H228 get separated in open states, with $_{H}$TM5-6 loop disordered but NuoCD loop remaining extended (ED Fig. 5a). In the closed state $_{H}$E220 flips out to form a salt bridge with invariant $_{CD}$R407, while $_{CD}$H228 interacts much closer with $_{CD}$D329 (ED Fig. 7b), stabilising the retracted NuoCD loop conformation and allowing Q_d binding. These concerted loop movements suggest that open-ready state may represent the enzyme ready to bind external Q (since no Q is observed in the cavity), while the open state represents the stage when Q has entered and bound in the Q_m site (observed in open states from most datasets), followed by transition to the closed state. Therefore, the open-ready state likely represents an additional, previously not resolved, intermediate in the catalytic cycle.

In the open *Ec*CI, due to disorder in the $_{A}$TM1-2 and $_{H}$TM5-6 loops, the Q cavity is clearly open to the cytoplasm (Fig. 1d). $_{A}$TM1-2 loop is completely disordered in the open state and is partly ordered in the open-ready state, but access to the cytosol from the cavity remains (ED Fig. 5f). In the closed state this loop is ordered and seals off the Q cavity with the area around $_{A}$S52 coming together with NuoH and NuoCD loops (Figs. 1e and 2b), fixed in place by two conserved salt bridges: $_{A}$K46-$_{H}$E71 and $_{A}$E51-$_{H}$K140 (ED Fig. 2h). $_{A}$S52 corresponds to $_{ND3}$Cys39 in mammals, a NEM-sensitive marker residue known to be buried in the closed state and exposed in the open or in the deactive state[3,82]. In the closed state this residue can interact with conserved $_{CD}$H224 and $_{H}$Y141, which helps to simultaneously close off the cavity and to keep NuoCD loop retracted.

8. A full description of the proposed coupling mechanism

The sequence of events in the proposed mechanism is as follows (Fig. 4). **(Step 1)** Much of the time the enzyme spends in the open (or open-ready) state, waiting for quinone from the membrane pool to enter and temporarily bind in the Q_m (bacterial) or Q_s (mammalian) site near the entrance. Site W is open for waters to flow out of the cavity and give space to the incoming quinone, while the Q cavity is expanded to allow for the unimpeded quinone entry. We propose that in this state the ALS are maximally protonated at the key *TM8* sites (Lys/HisTM8) by protons coming into NuoL/NuoM from the cytoplasm (or mitochondrial matrix) and redistributed along the central axis into NuoN and part of the E-channel harbouring $_{K}$E72 and $_{K}$E36 (for the ease of following proton transfers we indicate any protonated residues just by a "+" sign, leaving unprotonated ones empty). The rest of the E-channel is disconnected from this chain at $_{J}$TM3, preventing proton leak into the Q cavity and back to the cytosol. This may be important because protons are quite scarce in the cytosol. For the closely interacting *TM7/TM5* ion pair sites (LysTM7/GluTM5), the proton is proposed to reside in *TM5* site, as suggested by our observations in *Ec*CI (ED Fig. 7c) and *Oa*CI (if only the density of glutamates is considered[3]). The residues in *TM7/TM5* ion pairs are thus uncharged. The *TM12* (Lys/GluTM12) sites are proposed to have a lower *pK*a and tuned to remain unprotonated in this state due to electrostatic interactions with protonated *TM8* and *TM5* sites. The exception is NuoL *TM12* site, proposed to be protonated as it is distal and so does not have a *TM5* partner from a neighbouring subunit. **(Step 2)** Bound quinone traverses into the Q_d site, triggering the open-to-closed transition, so that the W site is closed off and the Q cavity tightly engulfs quinone. $_{J}$TM3 rotates, establishing the uninterrupted proton path from the Q cavity all the way to MA tip. Quinone accepts two

electrons from cluster N2 in quick succession[13], and the unstable charged quinone intermediate is immediately protonated by the coordinating $_{CD}$H228/$_{CD}$D329, creating a double negative (relative to the previous state) charge in the area. Since the Q cavity is sealed, the protons for the re-protonation of $_{CD}$H228/$_{CD}$D329 come from the central axis. The available redox energy from quinone chemistry appears to be sufficient to displace at least four ($_{H}$E157, $_{A}$D79, $_{K}$E36 and $_{N}$E133 (ED Fig. 7c)) protons along the central axis, as they are not transferred against the pmf. Two of these are substrate protons and the rest may be shifted towards the Q site to enhance the charge action signal near NuoN. **(Step 3)** In a "minimal" interpretation (Occam's razor) of the subsequent events, de-protonation of the E-channel residues (and $_{N}$E133) first triggers proton transfer from *TM8* to *TM7* site in NuoN, due to the removal of large positive charge around *TM5* area. In a series of "domino effect" events, the removal of $_{N}$*TM8* charge allows $_{M}$*TM5* proton to hop on $_{N}$*TM12* site, repeated in NuoM/L by $_{M}$*TM8* to $_{M}$*TM7*, $_{L}$*TM5* to $_{M}$*TM12* and $_{L}$*TM8* to $_{L}$*TM7* hops. De-wetting of the *TM8* area due to de-protonation, as observed in MD simulations[11], would prevent the back-flow of protons. Effectively, due to the "forcefully" protonated *TM12* sites and a shift of proton from *TM5* to *TM7* sites (so that the residues in *TM7/TM5* ion pairs are now charged) the enzyme will now be in a highly energised state, akin to a loaded spring or stacked dominos ready to fall. **(Step 4)** The presence of the freshly produced quinol in the Q_d site along with the re-protonated state of coordinating residues triggers the transition from the closed to the open state, so that the Q cavity widens and the W site opens, allowing waters to come in and help quinol on its way out. The *TM8* sites (and $_{K}$E72/E36) can be fully protonated from the cytosol, blocked off from the Q cavity by $_{J}$TM3. In total at this stage six protons (four to be pumped and two substrate) will enter the central axis. Five of them can enter via NuoL/M, re-distributed along the central axis, while $_{H}$D79 can be protonated via open Q cavity. In this scenario the re-protonation of *TM8* sites (and $_{K}$E72/E36) is rather "passive", the key to coupling being that *TM12* and *TM7/TM5* sites state is fully controlled by quinone reactions. **(Step 5)** Electrostatic interactions with the protonated *TM8* and *TM7* sites (red dashes in Step 4) lead to a large decrease of *pK*a's of *TM12* residues, forcing them to lose their protons. In NuoL the *TM12* proton would be ejected directly into the periplasm (or mitochondrial IMS). In the reverse wave of the "domino effect" (exact sequence of events is given at the end of this paragraph) this will initiate a sequence of proton hops from $_{L}$*TM8* to $_{L}$*TM12*, $_{L}$*TM7* to $_{L}$*TM8* and $_{M}$*TM12* to $_{L}$*TM5*, repeating twice more in NuoM/N and ending with $_{K}$E72 donating proton to $_{N}$*TM5*. The simple natural basis for this transfer of protons along the central axis is the appearance of a "vacancy" on the "left" of the chain and

the electrostatic "pressure" of the incoming proton from the "right" (or reverse in Step 3). Effectively, after the cycle is repeated three times, each time ending closer to NuoL, in the end the $_{M}$*TM12*, $_{N}$*TM12* and $_{K}$E72 sites would transfer their protons along the central axis towards NuoL, adding up with the initial $_{L}$*TM12* to the four protons ejected into the periplasm. This brings the system back to Step 1, with *TM8* protonated and a proton in *TM7/TM5* "switch" sitting again on *TM5*, thus the cycle re-starts. Crucially, for the mechanism to work, a *TM12* proton from NuoN/M must be transferred to the neighbouring NuoM/L *TM5* and not directly to the periplasm, as otherwise the process will not be initiated in the next subunit (i.e. a domino will fall without tripping the next one). Similarly, in Step 3 it is essential for protons to hop across subunit interfaces from *TM5* to *TM12* sites. Therefore, our mechanism naturally explains initially counter-intuitive NuoL-only exit. The pump works with protons moving along the entire central axis either towards Q cavity (Steps 2-3) or in the reverse wave (Step 5), thus the periplasm/IMS side must be shielded from the solvent everywhere except the NuoL exit.

After a prolonged absence of turnover the enzyme enters a resting (bacterial) or a deactive (mammalian) state, which may help to prevent ROS production, occurring *via* reverse electron transport in specific conditions, such as ischaemia-reperfusion injury[83]. When turnover resumes the enzyme reverts back to the main cycle.

The mechanism also explains the reverse electron transport in complex I: high pmf would promote reverse reaction by driving charge transitions in ALS in reverse to those in Fig. 4. Translocation of protons into the matrix would be coupled to transfer of protons from the Q coordinating residues into the central axis, creating a negative charge near Q_d site. It would promote quinol binding and oxidation, as well as lower the N2 redox potential, enabling reverse electron transfer from N2 to FMN and NAD^+.

Structurally observed (under turnover) states of *Ec*CI likely represent, for the open states a mixture of Steps 1, 4 and 5 in Fig. 4; and for the closed state - a mixture of Steps 2-3. The mixtures would be present because apart from protonation state these states do not substantially differ and so cannot be resolved by 3D classification. This probably explains why we do not see a clear change in protonation states of $_{M}$GluTM5, $_{M}$GluTM12 and $_{L}$GluTM5, in contrast to E-channel residues (which are charged in Steps 2 and 3).

For clarity and to help understanding, below we provide a full sequence of events during proton ejection (Step 5).

Here we use signs 0 or + to indicate an unprotonated and protonated residue, respectively (of course the actual charge will differ depending on residue as noted in Fig. 4 legend). After the first proton from $_{L}$*TM12* is released into IMS/periplasm (1 H^+ pumped so far), and a sequence of proton hops from $_{L}$*TM8* to $_{L}$*TM12*, $_{L}$*TM7* to $_{L}$*TM8* and $_{M}$*TM12* to $_{L}$*TM5*, repeating twice more in NuoM/N and ending with $_{K}$E72 donating proton to $_{N}$*TM5*, the situation will be as follows, with protonation state of key TM12, TM8, TM7, TM5 residues in antiporters and $_{K}$E72/E36 in the E-channel, respectively:

L (++0+), M (++0+), N(++0+), E-channel (0+).

At this stage the freshly arrived $_{M/N}$*TM12* protons will push $_{L/M}$*TM5* protons onto $_{L/M}$*TM7*. This will re-create the state of NuoL exactly as it was at step 4 and so will push $_{L}$*TM12* proton out (2 H^+ pumped by now). This again initiates a sequence of proton hops from $_{L}$*TM8* to $_{L}$*TM12*, $_{L}$*TM7* to $_{L}$*TM8* and $_{M}$*TM12* to $_{L}$*TM5*, repeating twice more in NuoM/N, and ending now with $_{K}$E36 donating proton to $_{N}$*TM5*, which will create the following distribution:

L (++0+), M (++0+), N(++0+), E-channel (00).

Another repeat of the steps just above (3 H^+ pumped by now), but now ending with $_{N}$*TM12* donating proton to $_{M}$*TM5*, will result in the following distribution:

L (++0+), M (++0+), N(0+0+), E-channel (00).

Finally, another repeat of the steps above (4 H^+ pumped at this stage, accounting for full stoichiometry), but now ending with $_{M}$*TM12* donating proton to $_{L}$*TM5*, will result in the following distribution, i.e. the end of Step 5 as depicted in Fig. 4:

L (++0+), M (0+0+), N(0+0+), E-channel (00).

Both $_{K}$E36 and $_{K}$E72 can donate protons to $_{N}$*TM5* due to arrival of positive charge to $_{A}$D79 and $_{H}$E157 in the open state – these residues are close enough to interact electrostatically even when $_{J}$TM3 bridge is blocked (as in the open state).

9. Discussion of alternative proposals.

In some recent publications, an alternative path for substrate protons from the cytosol to the Q site was proposed at or near the W site discussed here. It involved either the transfer via specific residues in this area[17] or via the branching cavity (similar to cavity leading towards W site) in a gated fashion to allow access of substrate protons instead of waters[84]. It is important to note that such a pathway for substrate protons would render them useless for coupling, as the redox reaction would be essentially equilibrated with the cytosol. Only the existence of a very strong and very specific conformational gate linking the Q cavity to all

the antiporters would make such a mechanism feasible. However, neither mammalian nor bacterial enzymes show any conformational changes in any of the three ALS under turnover, rendering coupling to quinone protonation via any pathway to the cytosol near PA unlikely. Furthermore, even though there are plenty of charged residues linking the Q cavity to the E-channel, the quinone headgroup in the Q_d site is otherwise well shielded by hydrophobic residues, except for the coordinating residues. In general, however, this area is relatively hydrophilic as needed for the closed-to-open transition, when NuoA/H loops become exposed to the cytoplasm.

In a recent report, our proposal for ND5/NuoL-only outlet into periplasm was supported on the basis of the structures and MD studies on *Yl*CI[20]. However, the coupling mechanism proposed by the authors involved substrate proton access near the PA interface, which would not allow gating, as noted above. Furthermore, the role for shuttling of the charged quinone intermediates was proposed, which is unlikely due to the extremely short lifetime of such intermediates[85,86]. Moreover, only one conformational state was observed under turnover conditions, while clearly at least two are necessary for any coupling mechanism to work. The one observed *Yl*CI turnover state resembles the open state of *Oa*CI as similar areas (such as ⱼTM3-4 and ND3/NuoA loops) are disordered (but ordered in closed *Oa*CI). Therefore, the reported conformational changes in *Yl*CI may reflect the deactive to open state transition. The failure to observe, so far, a closed state in *Yl*CI could be because it is a high-energy state in enzymes which do not show the apo closed-like state, such as *Ec*CI and *Yl*CI (in contrast to mammalian). More extensive 3D classification (e.g. by focus-revert-classify approach as used here, see Methods) or different data collection strategies may be required to resolve this class in *Yl*CI.

In a recent MD study hydration profiles consistent with ND5-only proton exit were observed in several species, although the interpretation was different[11]. In another recent report[21] the proposed mechanism involved a key role of the enclosed Q cavity, similar to our arguments, but the rest of mechanism was very vague (in part because only the resting state of *Ec*CI was resolved) and also involved hypothetical conformational changes in the antiporters (which do not happen as we have shown).

A recent publication claimed to overturn our earlier mechanism of complex I[3] and suggested yet another alternative[19], based on a permanently bound ubiquinone shuttling electrons from the deep to the shallow binding site, where they get transferred to a hypothetical loosely bound external molecule of ubiquinone. This proposal is inconsistent with the current knowledge on complex I and the authors do not present any experimental

evidence for the binding of an external quinone. On the contrary, there are no clear potential binding sites on the protein surface near Q entry point (even though such sites were computationally predicted recently, they appear to be too far from the Q_s site for efficient electron transfer[87]). The authors[19] invoke comparison to Photosystem II (PSII) where primary acceptor Q_A donates electrons to Q_B. However, in PSII, a non-heme Fe (within iron-quinone complex) promotes electron tunnelling between the quinones[88], a feature clearly absent in complex I. There is also no proposal on how protons released from internal quinone would lead to proton translocation. In fact, the main new data in the report was the mode of Q10 binding, while the other structural findings are similar but cover less ground (e.g. there are no turnover conditions) than already published[3]. Further, the authors reiterated the assignment of the open and closed conformations to the deactive and active states, respectively, without providing any new data for this claim and using the same reasoning which we discussed and dismissed previously[3], above and in our recent review[89]. Another argument was that in the open state quinone cannot bind in the deep site and that the connection between the Q cavity and ALS is interrupted. However, these are exactly the features which allow the open state to act as part of the catalytic cycle in our mechanism. In summary, there is no experimental basis for the mechanistic proposals in this report[19].

Supplementary Discussion References

57 Schimpf, J. *et al.* Structure of the peripheral arm of a minimalistic respiratory complex I. *Structure*, (2021).

58 Yip, C. Y., Harbour, M. E., Jayawardena, K., Fearnley, I. M. & Sazanov, L. A. Evolution of respiratory complex I: "supernumerary" subunits are present in the alpha-proteobacterial enzyme. *J. Biol. Chem.* **286**, 5023-5033, (2011).

59 de Vries, S., Dorner, K., Strampraad, M. J. & Friedrich, T. Electron tunneling rates in respiratory complex I are tuned for efficient energy conversion. *Angew Chem Int Ed Engl* **54**, 2844-2848, (2015).

60 Zu, Y., Di Bernardo, S., Yagi, T. & Hirst, J. Redox properties of the [2Fe-2S] center in the 24 kDa (NQO2) subunit of NADH:ubiquinone oxidoreductase (complex I). *Biochemistry* **41**, 10056-10069, (2002).

61 Birrell, J. A., Morina, K., Bridges, H. R., Friedrich, T. & Hirst, J. Investigating the function of [2Fe-2S] cluster N1a, the off-pathway cluster in complex I, by manipulating its reduction potential. *Biochem J.* **456**, 139-146, (2013).

62 Langen, R., Jensen, G. M., Jacob, U., Stephens, P. J. & Warshel, A. Protein control of iron-sulfur cluster redox potentials. *J Biol Chem* **267**, 25625-25627, (1992).

63 Euro, L., Bloch, D. A., Wikstrom, M., Verkhovsky, M. I. & Verkhovskaya, M. Electrostatic interactions between FeS clusters in NADH:ubiquinone oxidoreductase (Complex I) from Escherichia coli. *Biochemistry* **47**, 3185-3193, (2008).

64 Ingledew, W. J. & Ohnishi, T. An analysis of some thermodynamic properties of iron-sulphur centres in site I of mitochondria. *Biochem J.* **186**, 111-117, (1980).
65 Esterhazy, D., King, M. S., Yakovlev, G. & Hirst, J. Production of reactive oxygen species by complex I (NADH:ubiquinone oxidoreductase) from *Escherichia coli* and comparison to the enzyme from mitochondria. *Biochemistry* **47**, 3964-3971, (2008).
66 Grivennikova, V. G. & Vinogradov, A. D. Partitioning of superoxide and hydrogen peroxide production by mitochondrial respiratory complex I. *Biochim. Biophys. Acta* **1827**, 446-454, (2013).
67 Peng, G. *et al.* Identification and characterization two isoforms of NADH:ubiquinone oxidoreductase from the hyperthermophilic eubacterium Aquifex aeolicus. *Biochimica et biophysica acta. Bioenergetics* **1859**, 366-373, (2018).
68 Gostimskaya, I. S., Grivennikova, V. G., Cecchini, G. & Vinogradov, A. D. Reversible dissociation of flavin mononucleotide from the mammalian membrane-bound NADH: ubiquinone oxidoreductase (complex I). *FEBS Lett.* **581**, 5803-5806, (2007).
69 Gnandt, E., Schimpf, J., Harter, C., Hoeser, J. & Friedrich, T. Reduction of the off-pathway iron-sulphur cluster N1a of Escherichia coli respiratory complex I restrains NAD(+) dissociation. *Scientific reports* **7**, 8754, (2017).
70 Khaniya, U. *et al.* Hydrogen bond network analysis reveals the pathway for the proton transfer in the E-channel of T. thermophilus Complex I. *Biochimica et biophysica acta. Bioenergetics*, 148240, (2020).
71 Lee, Y. *et al.* Ion transfer mechanisms in Mrp-type antiporters from high resolution cryoEM and molecular dynamics simulations. *bioRxiv*, 2022.2001.2024.477492, (2022).
72 Tocilescu, M. A. *et al.* The role of a conserved tyrosine in the 49-kDa subunit of complex I for ubiquinone binding and reduction. *Biochim. Biophys. Acta* **1797**, 625-632, (2010).
73 Sato, M., Sinha, P. K., Torres-Bacete, J., Matsuno-Yagi, A. & Yagi, T. Energy transducing roles of antiporter-like subunits in Escherichia coli NDH-1 with main focus on subunit NuoN (ND2). *J Biol Chem* **288**, 24705-24716, (2013).
74 Uno, S. *et al.* Oversized ubiquinones as molecular probes for structural dynamics of the ubiquinone reaction site in mitochondrial respiratory complex I. *J Biol Chem* **295**, 2449-2463, (2020).
75 Parey, K. *et al.* High-resolution cryo-EM structures of respiratory complex I: Mechanism, assembly, and disease. *Science advances* **5**, eaax9484, (2019).
76 Bridges, H. R. *et al.* Structure of inhibitor-bound mammalian complex I. *Nature communications* **11**, 5261, (2020).
77 Zhou, L., Maldonado, M., Padavannil, A., Guo, F. & Letts, J. A. Structures of Tetrahymena's respiratory chain reveal the diversity of eukaryotic core metabolism. *Science*, eabn7747, (2022).
78 Cabrera-Orefice, A. *et al.* Locking loop movement in the ubiquinone pocket of complex I disengages the proton pumps. *Nature communications* **9**, 4500, (2018).
79 Kolata, P. & Efremov, R. G. Structure of Escherichia coli respiratory complex I reconstituted into lipid nanodiscs reveals an uncoupled conformation. *bioRxiv*, 2021.2004.2009.439197, (2021).
80 Kaila, V. R. & Hirst, J. Coupling mechanism of mammalian respiratory complex I remains elusive despite structural advances. *https://science.sciencemag.org/content/coupling-mechanism-mammalian-respiratory-complex-i-remains-elusive-despite-structural*, (2021).
81 Letts, J. A., Degliesposti, G., Fiedorczuk, K., Skehel, M. & Sazanov, L. A. Purification of Ovine Respiratory Complex I Results in a Highly Active and Stable Preparation. *J Biol Chem*, (2016).
82 Galkin, A. *et al.* Identification of the mitochondrial ND3 subunit as a structural component involved in the active/deactive enzyme transition of respiratory complex I. *J. Biol. Chem.* **283**, 20907-20913, (2008).

83 Chouchani, E. T. *et al.* Ischaemic accumulation of succinate controls reperfusion injury through mitochondrial ROS. *Nature* **515**, 431-435, (2014).
84 Galemou Yoga, E. *et al.* Essential role of accessory subunit LYRM6 in the mechanism of mitochondrial complex I. *Nature communications* **11**, 6008, (2020).
85 Efremov, R. G. & Sazanov, L. A. The coupling mechanism of respiratory complex I - A structural and evolutionary perspective. *Biochim. Biophys. Acta* **1817**, 1785-1795, (2012).
86 Wright, J. J., Fedor, J. G., Hirst, J. & Roessler, M. M. Using a chimeric respiratory chain and EPR spectroscopy to determine the origin of semiquinone species previously assigned to mitochondrial complex I. *BMC biology* **18**, 54, (2020).
87 Djurabekova, A. *et al.* Docking and molecular simulations reveal a quinone binding site on the surface of respiratory complex I. *FEBS Lett.*, (2022).
88 Shevela, D., Eaton-Rye, J. J., Shen, J. R. & Govindjee. Photosystem II and the unique role of bicarbonate: a historical perspective. *Biochim. Biophys. Acta* **1817**, 1134-1151, (2012).
89 Kampjut, D. & Sazanov, L. A. Structure of respiratory complex I - An emerging blueprint for the mechanism. *Curr. Opin. Struct. Biol.* **74**, 102350, (2022).

DDM_Apo dataset processing

1. Preprocessing, picking, initial cleaning

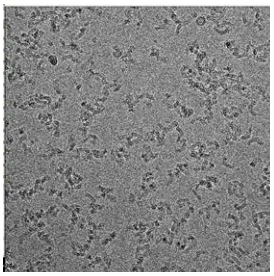

3652 movies

531k particles picked with gautomatch
525k particles picked with AutoPick
755k unique particles (duplicates removal within 70 Å)

One round of 2D and four rounds of 3D classifications

263k good particles

2. 3D classification

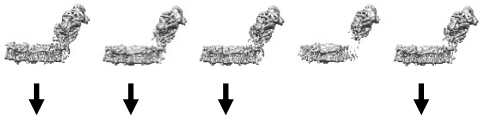

3. Refinement, polishing, CTF refinement

Extract at full size, auto-refine	3.87 Å
Ctf refinement, polishing	3.79 Å
Auto-refine – PA mask	3.28 Å

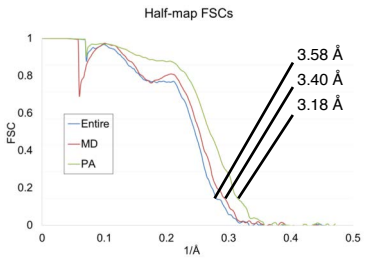

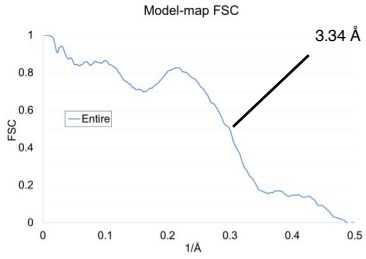

4. Focus-Revert-Classify 3D classification on PA-aligned map, loose membrane arm mask, no searches, T10

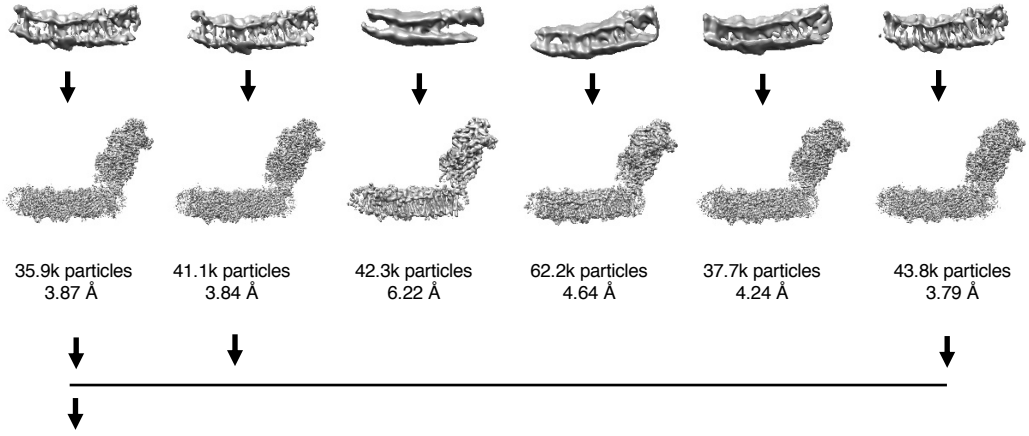

35.9k particles
3.87 Å

41.1k particles
3.84 Å

42.3k particles
6.22 Å

62.2k particles
4.64 Å

37.7k particles
4.24 Å

43.8k particles
3.79 Å

5. Autorefine
120903 particles
Consensus resting class
Entire 3.58 Å
PA: 3.18 Å
MA: : 3.40 Å

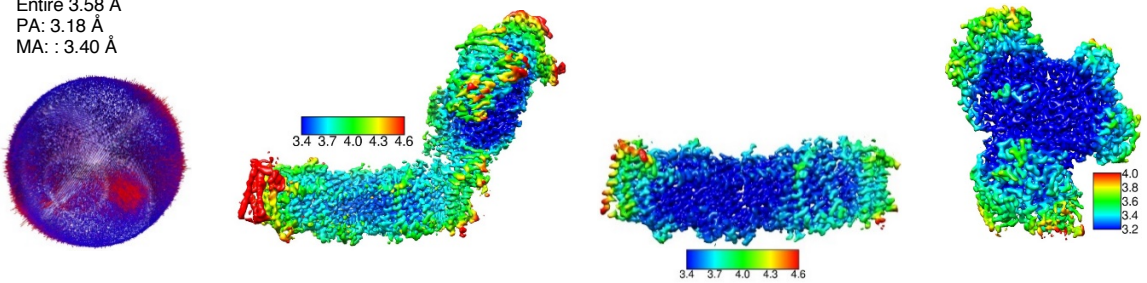

Figure S1

DDM_NADH dataset processing

1. Preprocessing, picking, initial cleaning

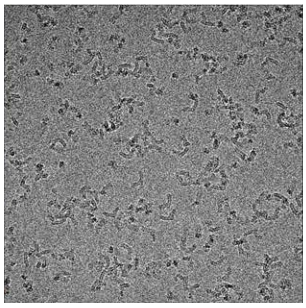

3028 good movies with CTF MaxRes < 5.5

303k particles picked with gautomatch
306k particles picked with AutoPick
441k unique particles (duplicates removal within 50 Å)

One round of 2D and 3D classifications

194k good particles

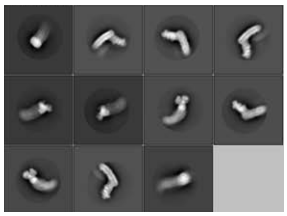

2. 3D classification

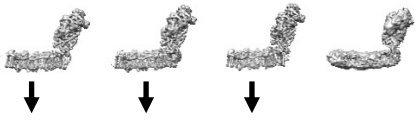

3. Refinement, polishing, CTF refinement

Extract at full size, auto-refine 3.58 Å

Ctf refinement, polishing 3.36 Å

Auto-refine – PA mask 2.98 Å

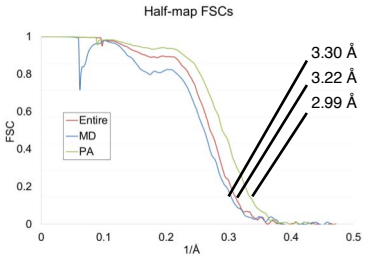

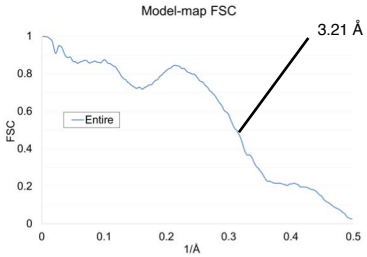

4. Focus-Revert-Classify 3D classification on PA-aligned map, loose membrane arm mask, no searches, T4

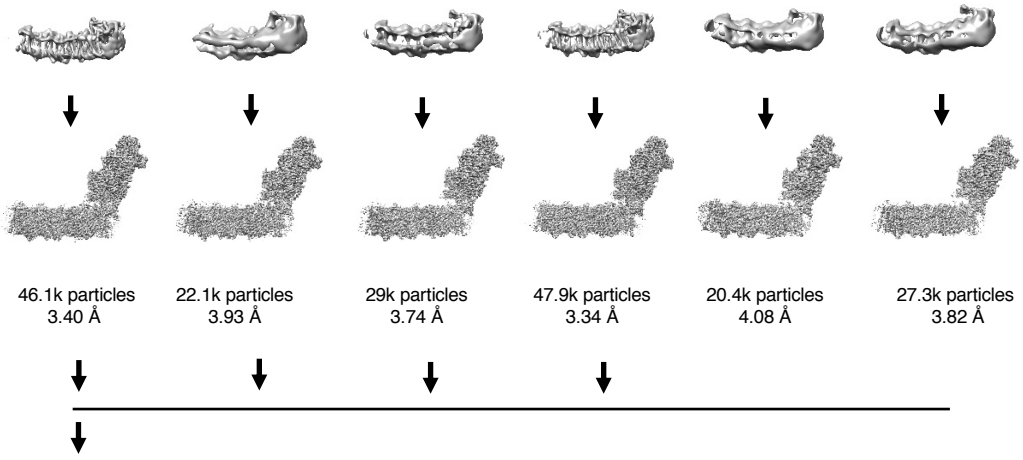

5. Autorefine
145253 particles
Consensus resting class
Entire 3.22 Å
PA: 2.99 Å
MA: : 3.30 Å

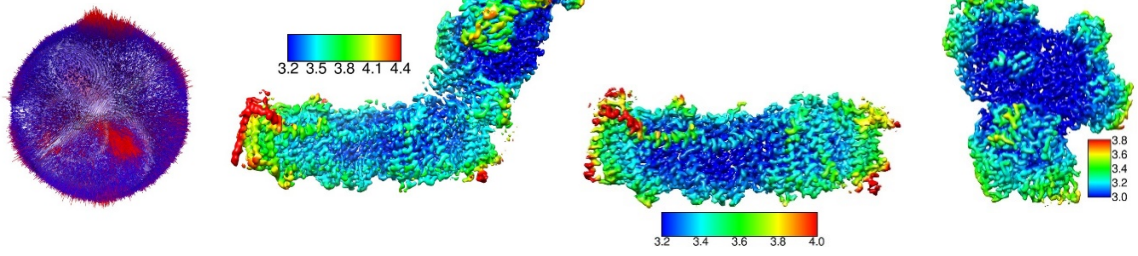

Figure S2

DDM/LMNG_Turnover_pH6 dataset processing

1. Preprocessing, picking, initial cleaning

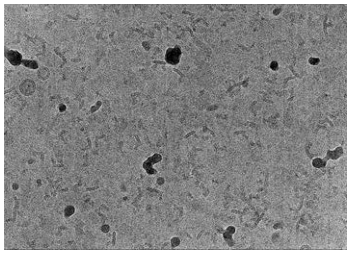

2656 good movies with Ctf MaxRes < 5

773k particles picked with AutoPick

One round of 2D and 3D classifications

268k particles

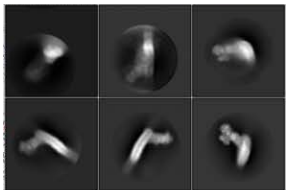

2. 3D classification

3. Refinement, polishing, CTF refinement

Extract at full size, auto-refine 3.26 Å

Ctf refinement, polishing 2.70 Å

Auto-refine – PA mask 2.32 Å

3D classification on focused PA, then on MD 204k clean particles

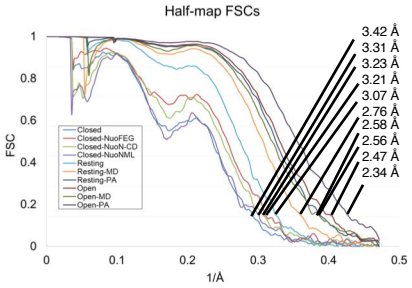

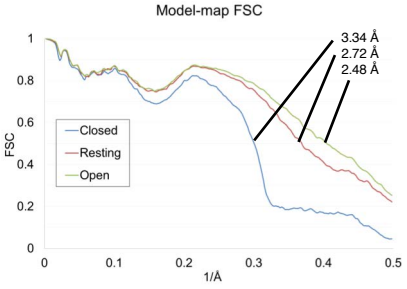

4. Focus-Revert-Classify 3D classification, loose membrane arm mask, no searches, T 4

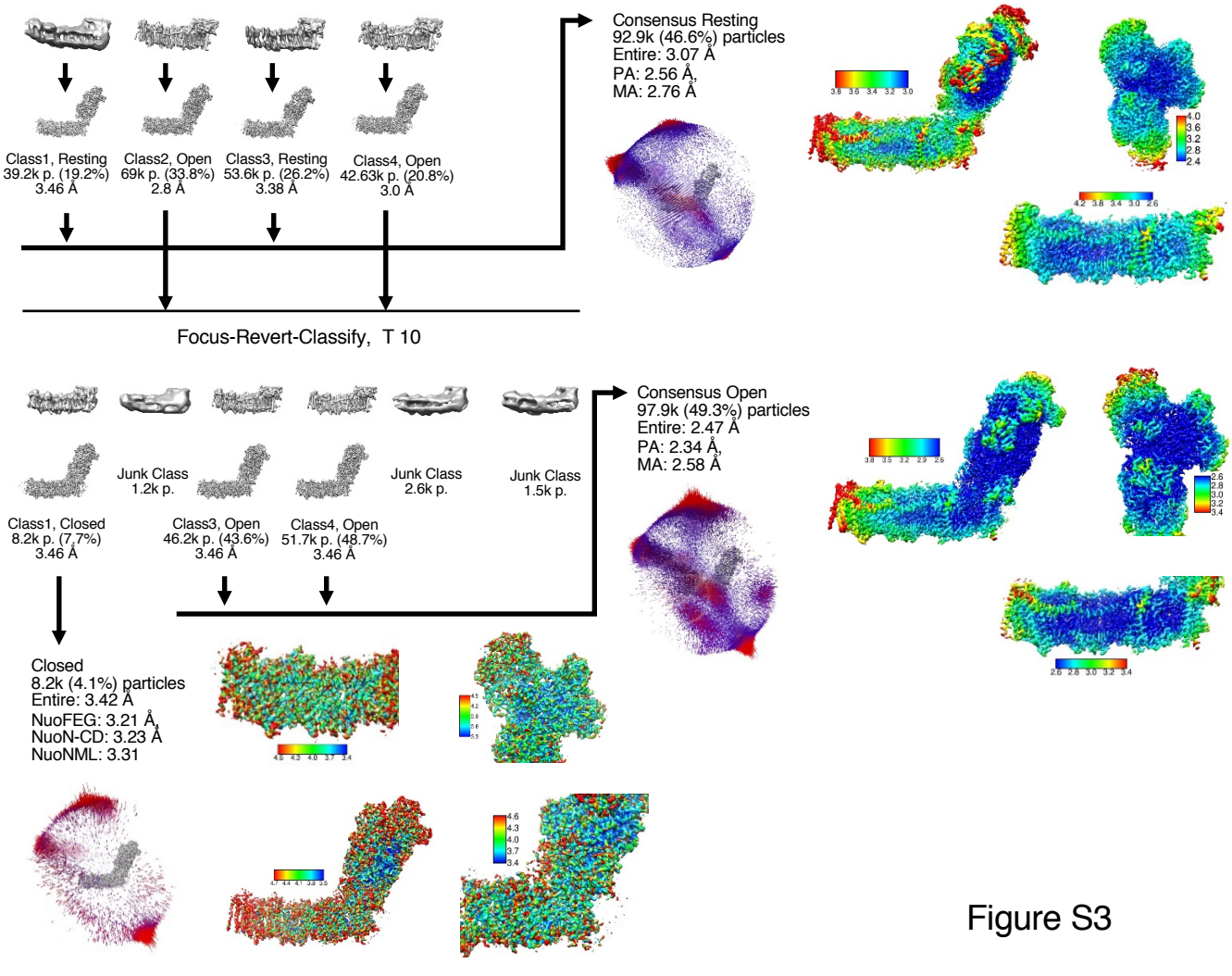

Figure S3

DDM/LMNG_Apo dataset processing

1. Preprocessing, picking, initial cleaning

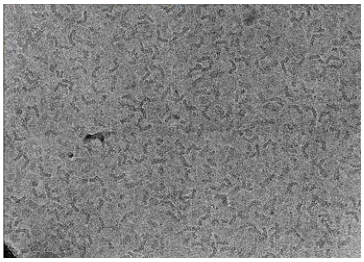

3415 good movies with Ctf MaxRes < 4

918k particles picked with AutoPick

Two round of 2D and one round of 3D classifications

387k particles

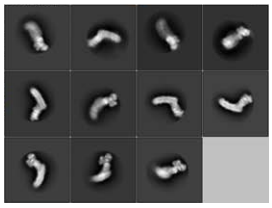

2. 3D classification

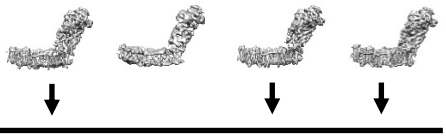

3. Refinement, polishing, CTF refinement

Extract at full size, auto-refine 3.24 Å

Ctf refinement, polishing 2.54 Å

Auto-refine – PA mask 2.21 Å

3D classification on focused PA, then on MD 366k clean particles

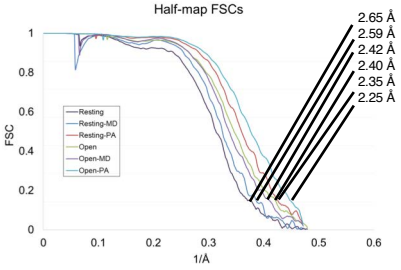

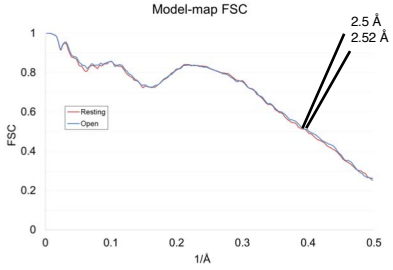

4. Focus-Revert-Classify 3D classification, loose membrane arm mask, no searches, T 4

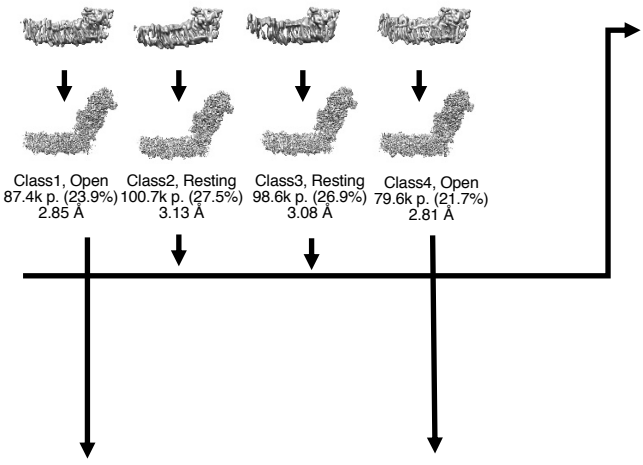

Consensus Resting
199.3k (54.4%) particles
Entire: 2.65 Å
PA: 2.35 Å,
MA: 2.59 Å

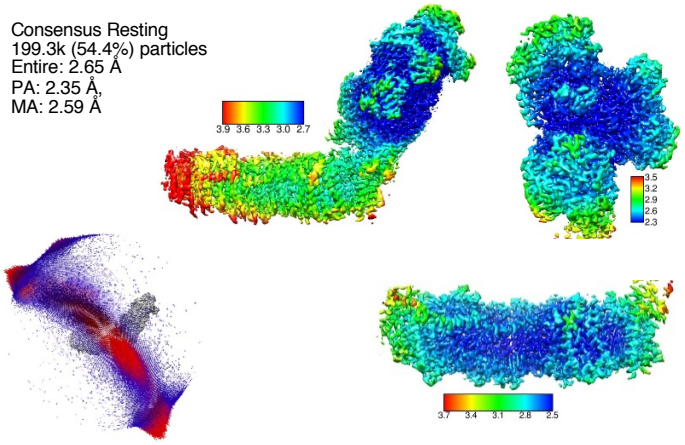

Consensus Open
167k (45.6%) particles
Entire: 2.40 Å
PA: 2.22 Å,
MA: 2.42 Å

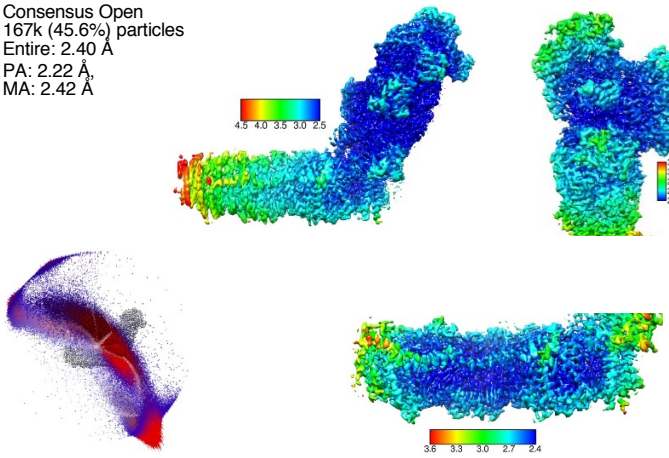

Figure S4

DDM/LMNG_PieA dataset processing

1. Preprocessing, picking, initial cleaning

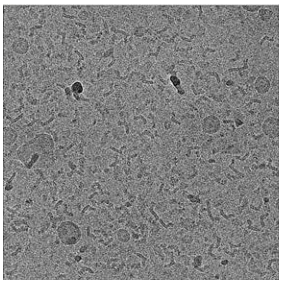

3394 good movies with Ctf MaxRes < 4

463k particles picked with gautomatch

Two rounds of 2D and one round of 3D classifications

233k particles

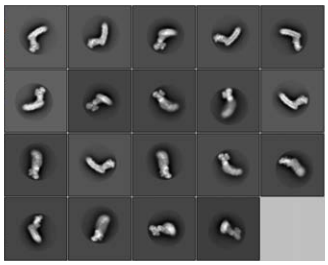

2. 3D classification

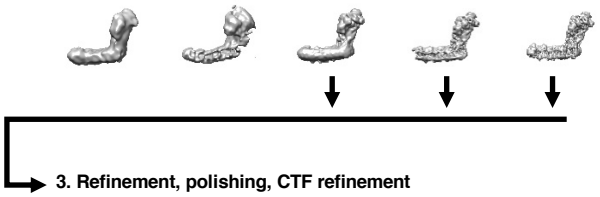

3. Refinement, polishing, CTF refinement

Extract at full size, auto-refine 3.84 Å

Ctf refinement, polishing 3.14 Å

Auto-refine – PA mask 2.95 Å

3D classification on focused PA, then on MD 214k clean particles

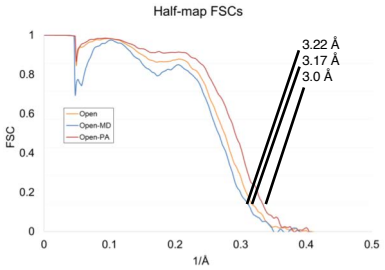

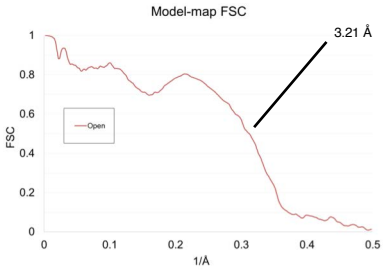

4. Focus-Revert-Classify 3D classification, loose membrane arm mask, no searches, T 4

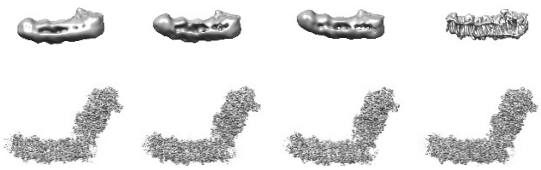

Class1,
Poor Resting
48.3k p. (22.6%)
4.1 Å

Class2,
Poor Resting
33.1k p.(15.5%)
4.1 Å

Class3,
Poor Resting
32.6k p. (15.2%)
4.2 Å

Class4, Open
99.9k p. (46.7%)

Open
99.9k (46.7%) particles
Entire: 3.17 Å
PA: 3.0 Å,
MA: 3.22 Å

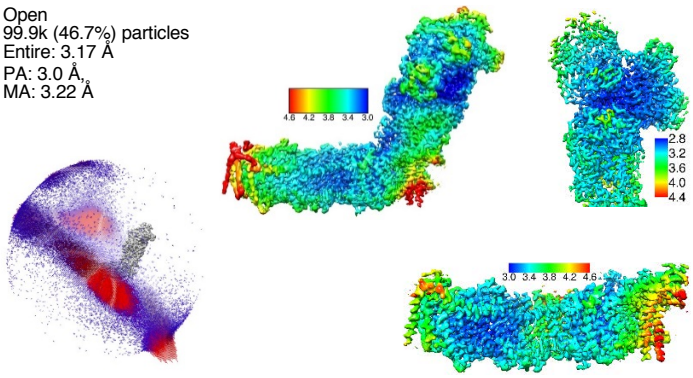

Figure S5

DDM/LMNG_NADH+FMN dataset processing

1. Preprocessing, picking, initial cleaning

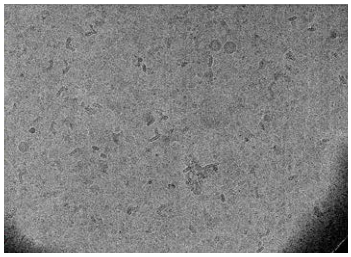

2602 good movies with Ctf MaxRes < 4.5

563k particles picked with AutoPick

One round of 2D and 3D classification

145k particles

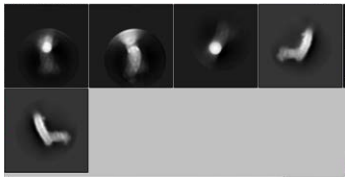

2. 3D classification

3. Refinement, polishing, CTF refinement

Extract at full size, auto-refine 3.62 Å

Ctf refinement, polishing 3.31 Å

Auto-refine – PA mask 2.94 Å

3D classification on focused PA, then on MD 122k clean particles

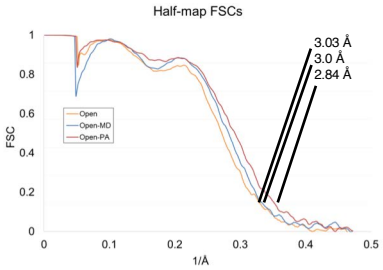

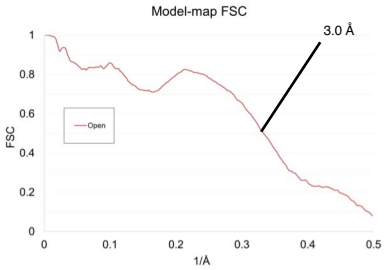

4. Focus-Revert-Classify 3D classification, loose membrane arm mask, no searches, T 4

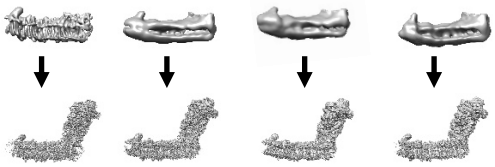

Class1, Open
36.8k p. (30%)

Class2,
poor Resting
22.8k p. (18.7%)
4.23 Å

Class3,
poor Resting
31k p. (25.4%)
5.04 Å

Class4,
poor Resting
31.4k p. (25.7%)
4.73 Å

Open
36.8k (30%) particles
Entire: 3.03 Å
PA: 2.84 Å,
MA: 3.0 Å

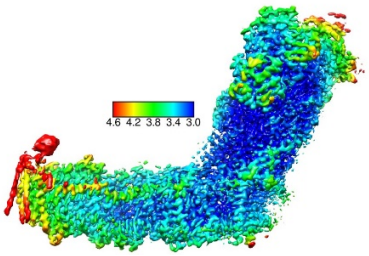

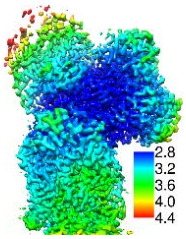

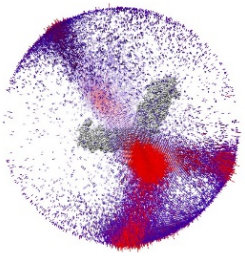

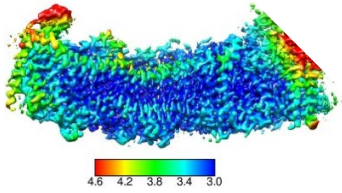

Figure S6

DDM/LMNG_DQ dataset processing

1. Preprocessing, picking, initial cleaning

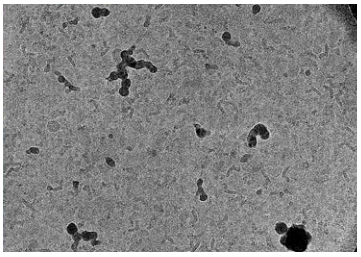

2744 good movies with Ctf MaxRes < 4.5

852k particles picked with AutoPick

Two rounds of 3D classification

137k particles

2. 3D classification

3. Refinement, polishing, CTF refinement

Extract at full size, auto-refine 3.33 Å

Ctf refinement, polishing 2.78 Å

Auto-refine – PA mask 2.43 Å

3D classification on focused PA, then on MD 123k clean particles

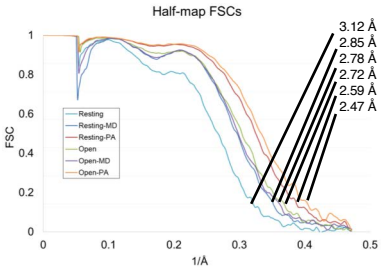

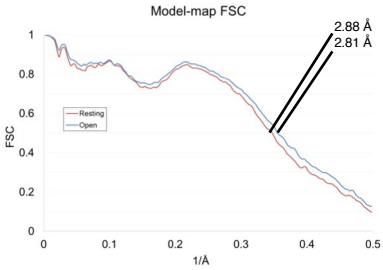

4. Focus-Revert-Classify 3D classification, loose membrane arm mask, no searches, T 4

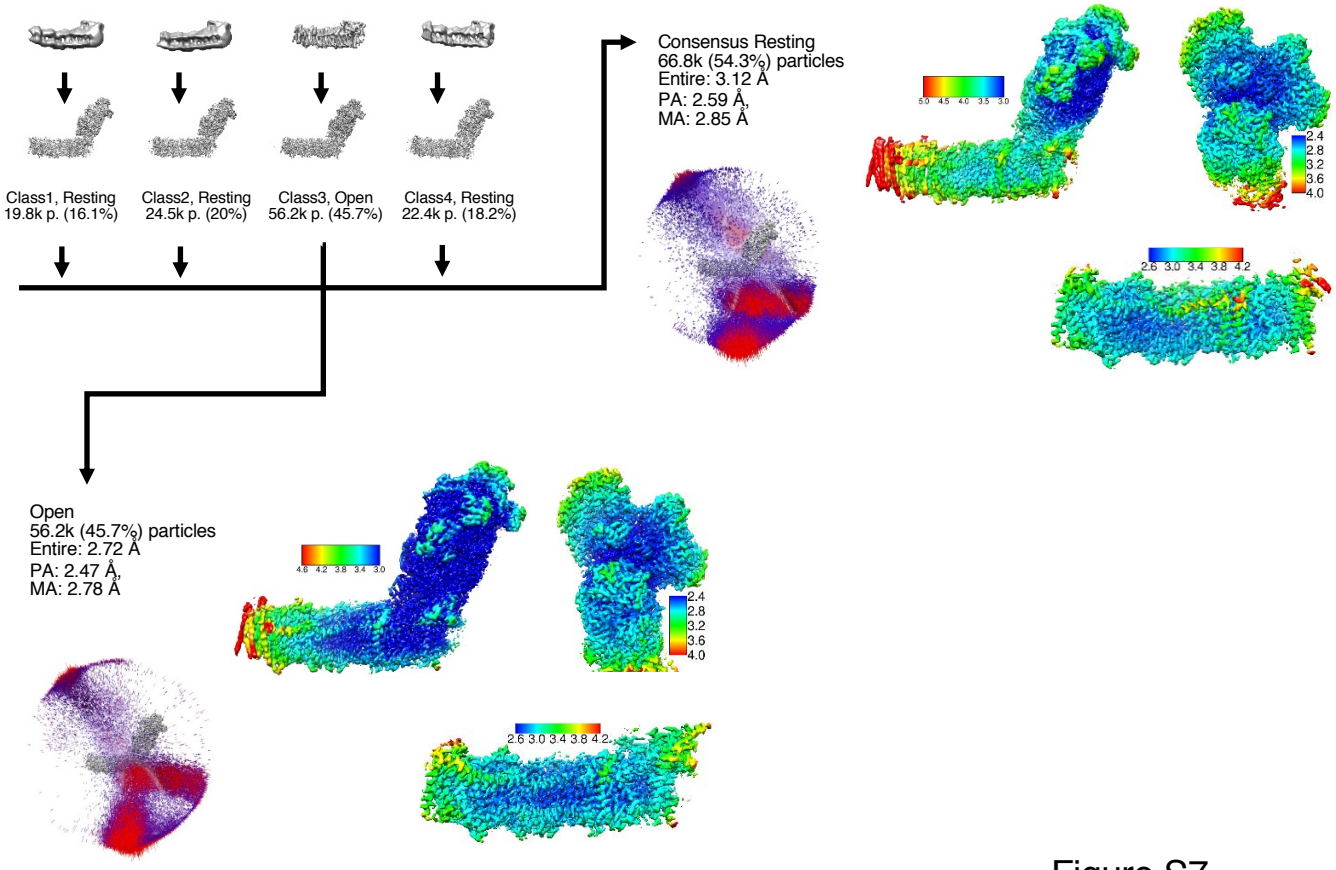

Figure S7

DDM/LMNG_Turnover_pH8 dataset processing

1. Preprocessing, picking, initial cleaning

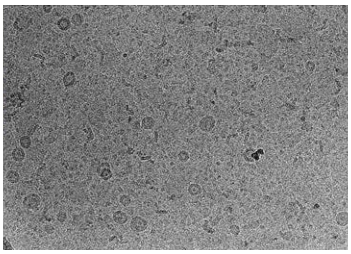

8271 good movies with Ctf MaxRes < 5

1.65 M particles picked with relion Autopick

One round of 2D and one round of 3D classifications

324k particles

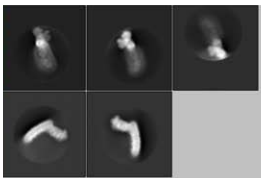

2. 3D classificaton

3. Refinement, polishing, CTF refinement

Extract at full size, auto-refine 3.2 Å

Ctf refinement, polishing 2.5 Å

Auto-refine – PA mask 2.3 Å

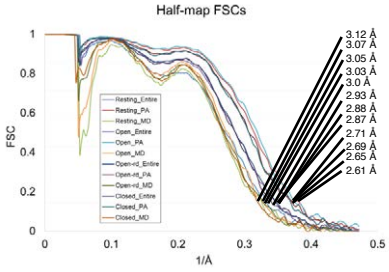

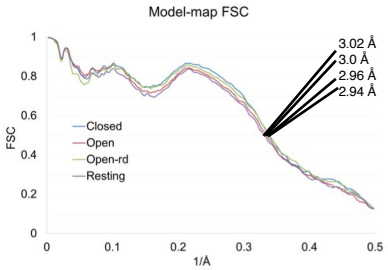

4. Focus-Revert-Classify 3D classification on PA-aligned map, loose membrane arm mask, no searches, T10

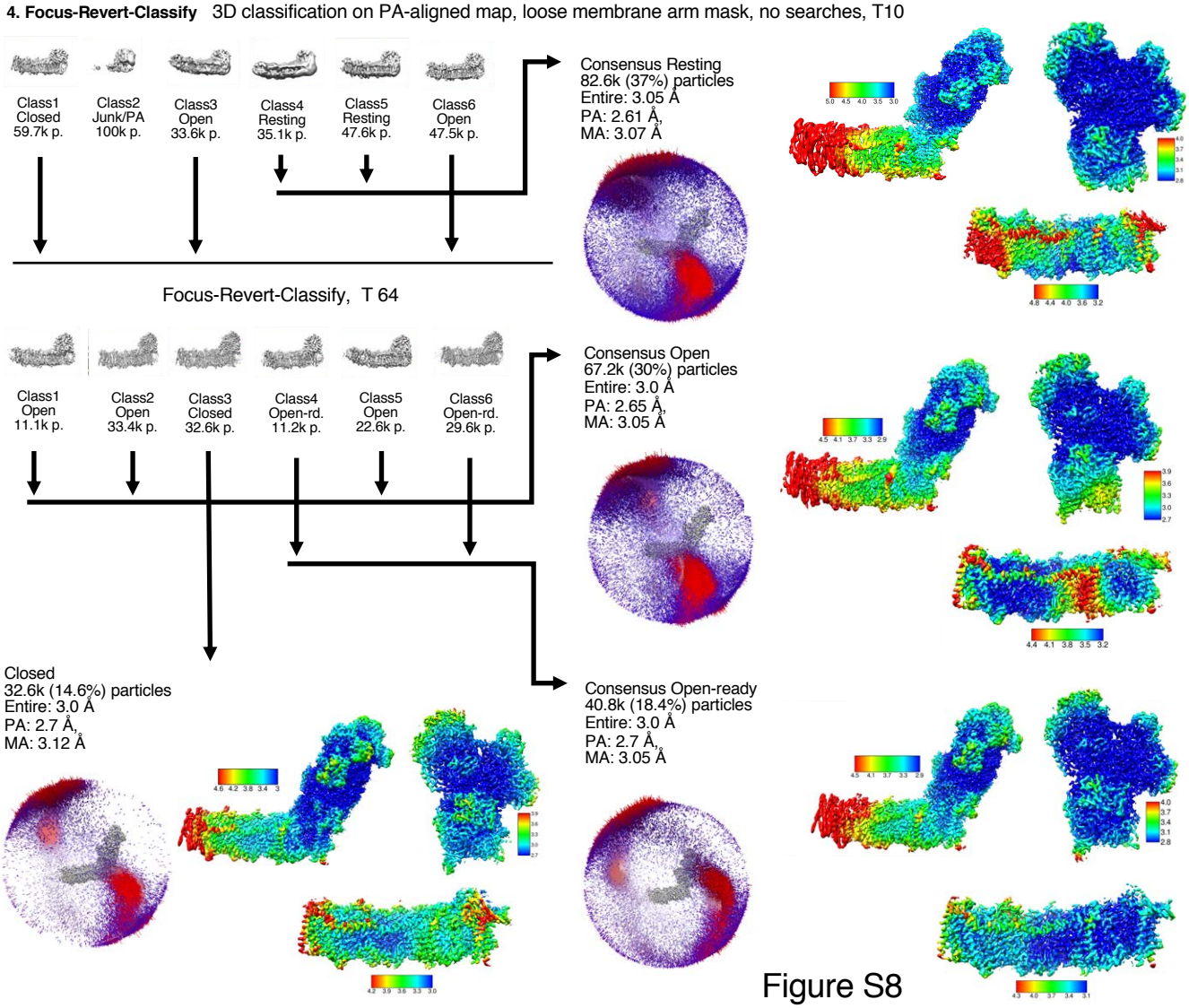

Figure S8

LMNG_Apo dataset processing

1. Preprocessing, picking, initial cleaning

4020 good movies with Ctf MaxRes < 5

1 M particles picked with relion Autopick

One round of 2D and one round of 3D classifications

240k particles

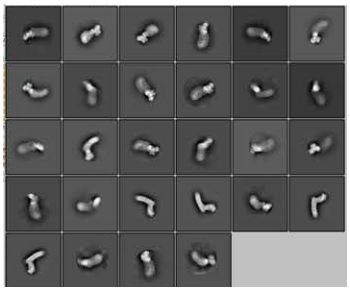

2. 3D classification

3. Refinement, polishing, CTF refinement

Extract at full size, auto-refine 3.9 Å

Ctf refinement, polishing 3.5 Å

Auto-refine – PA mask 3.1 Å

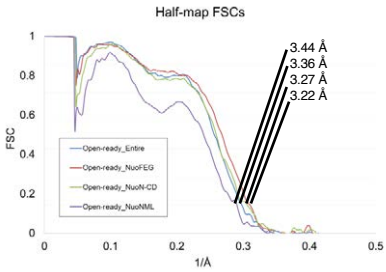

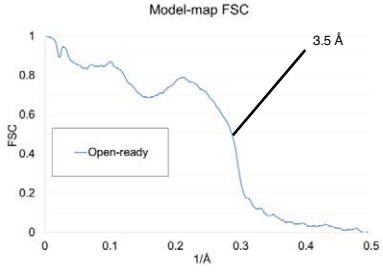

4. Focus-Revert-Classify 3D classification on PA-aligned map, loose membrane arm mask, no searches, T10

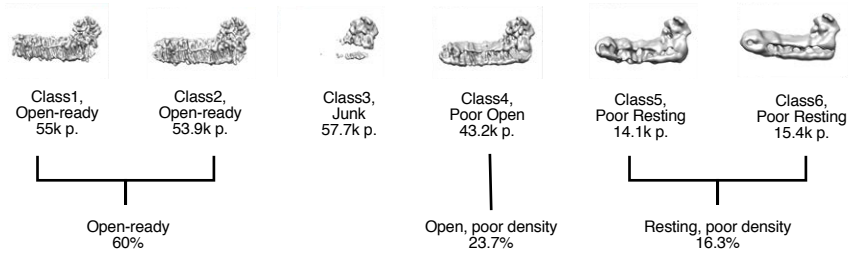

5. Autorefine

Open-ready
Entire: 3.4 Å
NuoFEG: 3.2 Å
NuoN-CD: 3.3 Å
NuoLMN: 3.4 Å

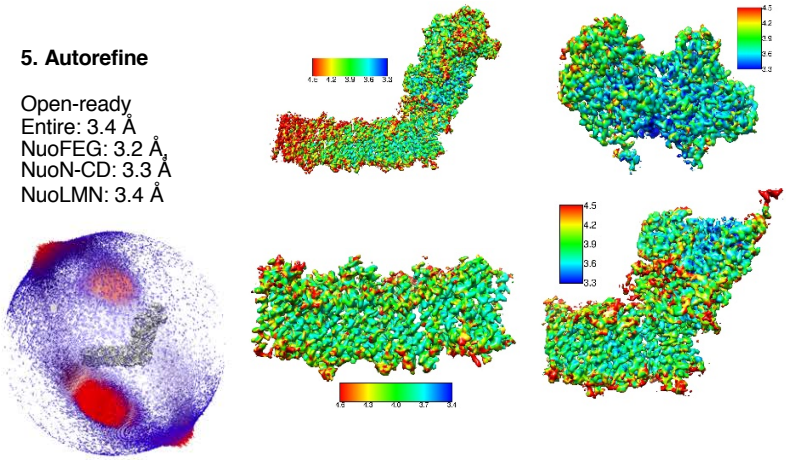

Figure S9

LMNG_Turnover dataset processing

1. Preprocessing, picking, initial cleaning

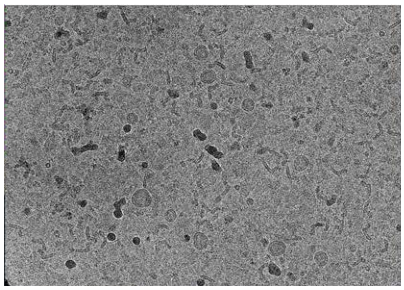

10285 good movies with Ctf MaxRes < 5

4.5 M particles picked with relion Autopick

One round of 2D and one round of 3D classifications

708k particles

2. 3D classification

3. Refinement, polishing, CTF refinement

Extract at full size, auto-refine 2.75 Å

Ctf refinement, polishing 2.24 Å

Auto-refine – PA mask 2.13 Å

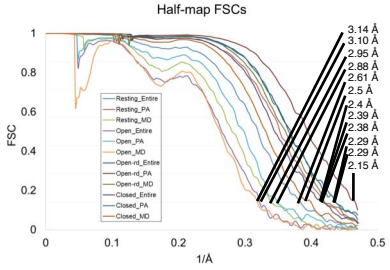

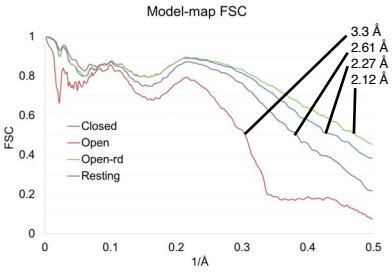

4. Focus-Revert-Classify 3D classification on PA-aligned map, loose membrane arm mask, no searches, T10

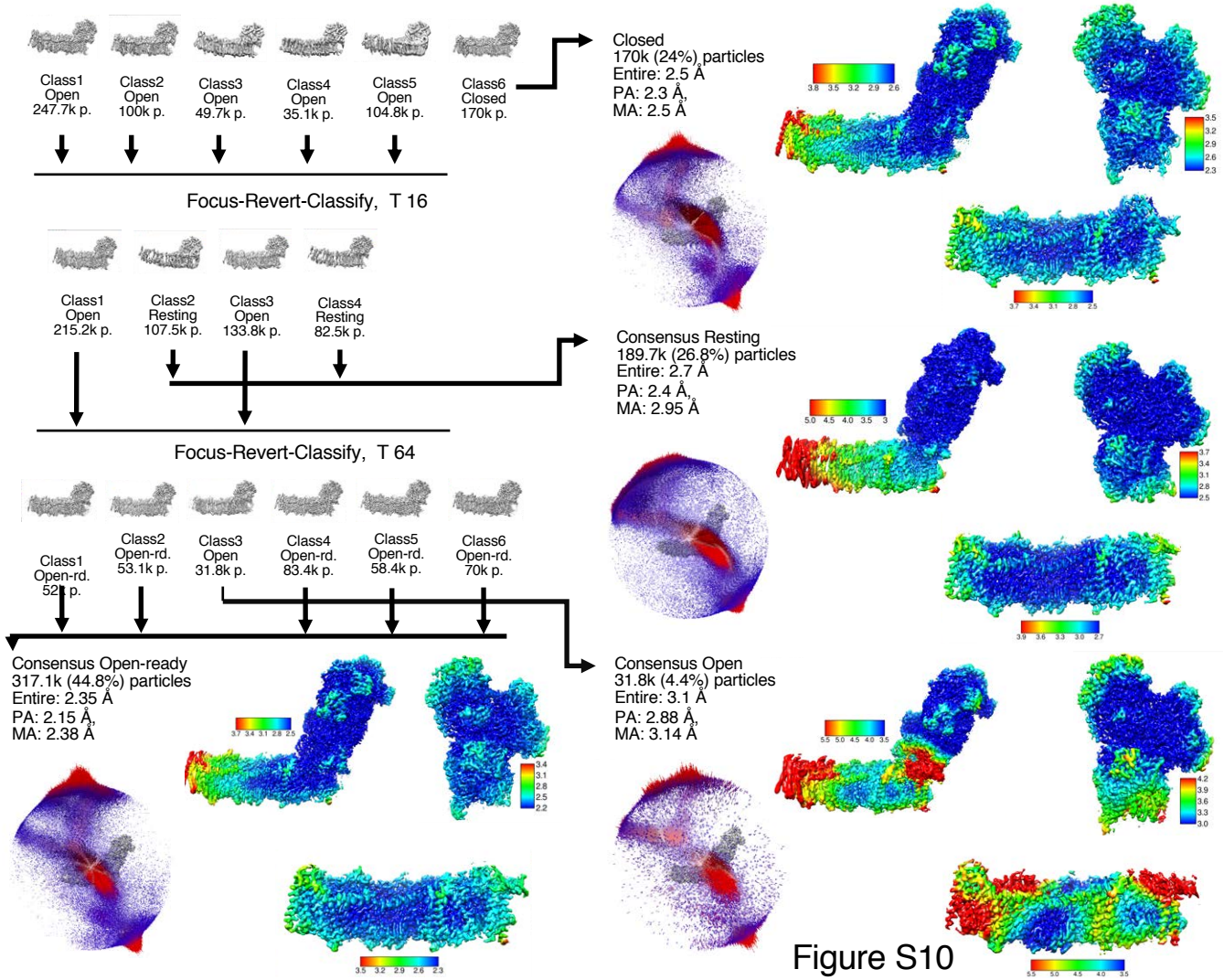

Figure S10

OvineCI_pH5.5 dataset processing

1. Preprocessing, picking, initial cleaning

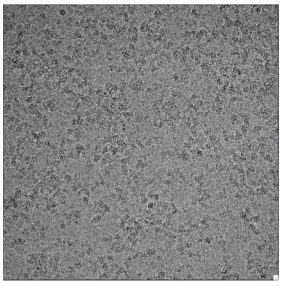

2097 good movies with Ctf MaxRes < 7

557664 particles picked with relion Autopick

One round of 2D classification, 540402 particles

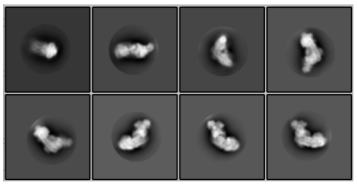

2. 3D classifications

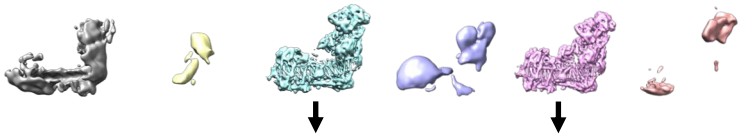

258453 selected particles

3. Refinement, polishing, CTF refinement

Extract classes #3 and #5 at full size, auto-refine 4.1 Å

Ctf refinement, polishing, Ctf refinement 3.4 Å

4. 3D classification without alignment, T8

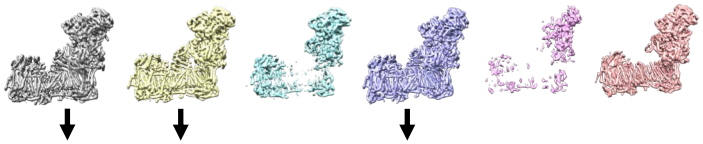

196583 selected particles

Auto-refine – PA mask 3.2 Å

5. Focus-Revert-Classify

3D classification on PA-aligned map, loose membrane arm mask, no searches, T16

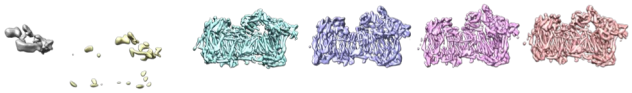

Class1 Junk/PA 60k p. | Class2 Junk 5.8k p. | Class3 Open2 46k p. | Class4 Open1 18.7k p. | Class5 Open3 32.8k p. | Class6 Closed 32.9k p.

Consensus open
97.5k (75%) particles
Entire: 3.3 Å
PA: 3.2 Å,
MA: 3.3 Å

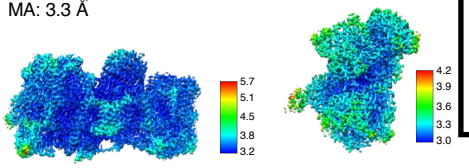

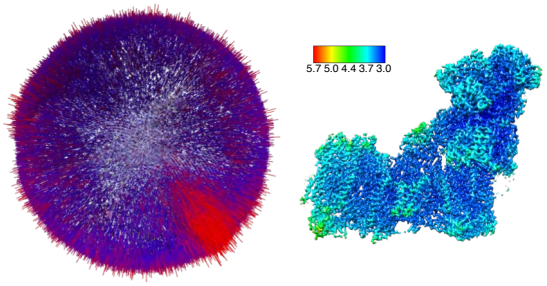

Consensus Closed
32.9k (25%) particles
Entire: 3.5 Å
PA: 3.4 Å,
MA: 3.5 Å

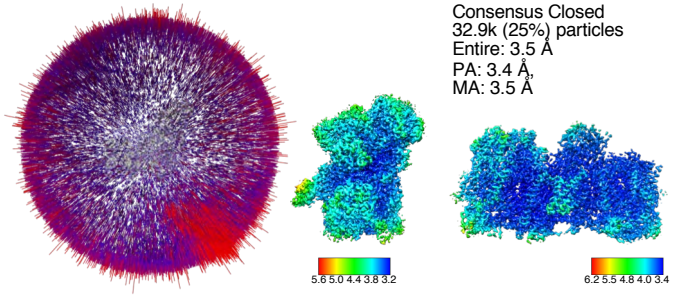

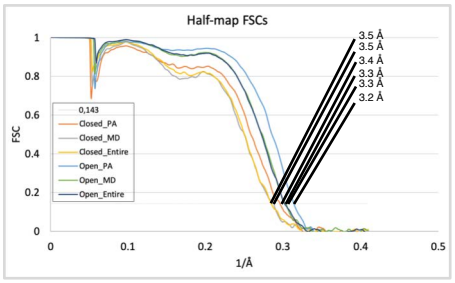

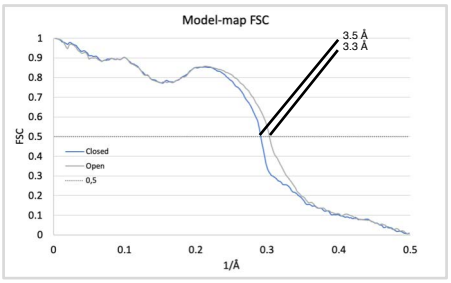

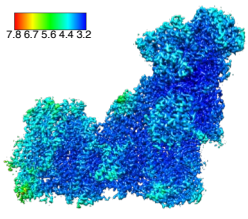

Figure S11

OvineCI_pH7.4 dataset processing

1. Preprocessing, picking, initial cleaning

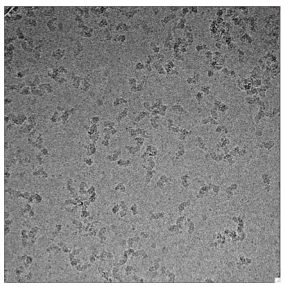

2931 good movies with Ctf MaxRes < 7

557585 particles picked with relion Autopick

One round of 2D classifications

547655 particles

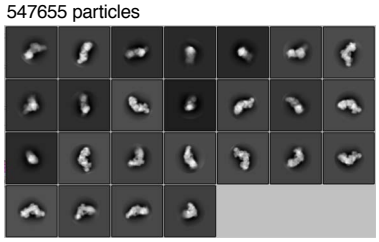

2. 3D classifications

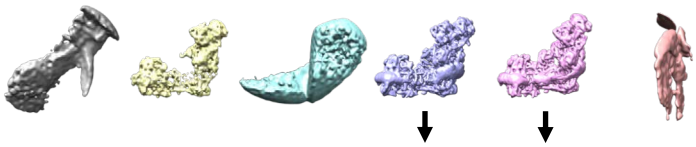

459315 selected particles

3. Refinement, polishing, CTF refinement

Extract at full size, auto-refine	3.75 Å
Ctf refinement, polishing, Ctf refinement	3.29 Å

4. 3D classification without alignment, T8

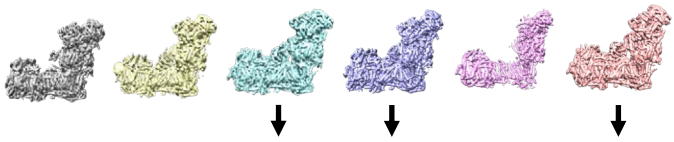

202246 selected particles

Auto-refine – PA mask 3.2 Å

5. Focus-Revert-Classify

3D classification on PA-aligned map, loose membrane arm mask, no searches, T16

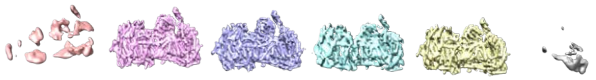

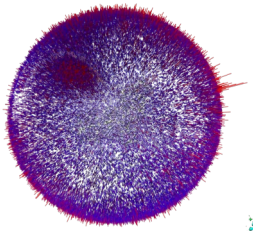

Closed
50.8k (31%) particles
Entire: 3.5 Å
PA: 3.4 Å,
MA: 3.5 Å

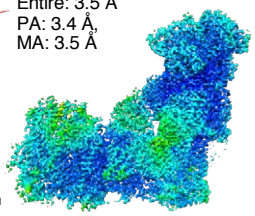

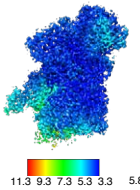

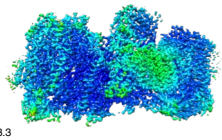

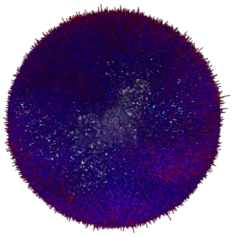

Consensus Open
82.6k (69%) particles
Entire: 3.2 Å
PA: 3.1 Å,
MA: 3.2 Å

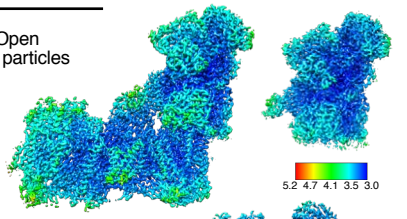

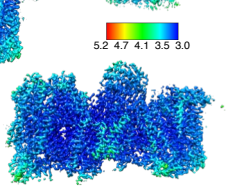

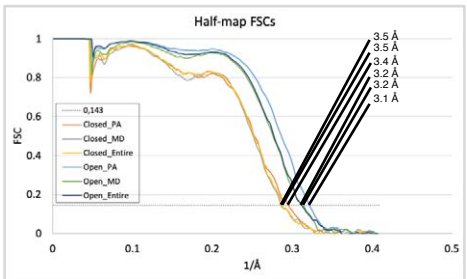

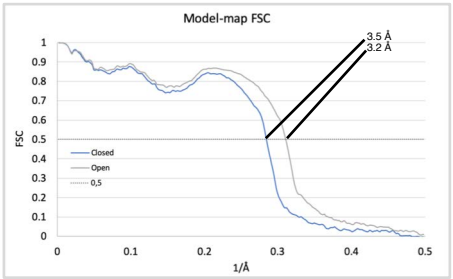

Figure S12

OvineCI_pH9 dataset processing

1.Preprocessing, picking, initial cleaning

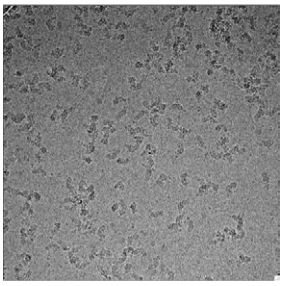

2799 good movies with Ctf MaxRes < 7

660526 particles picked with relion Autopick

One round of 2D classification

615876 particles

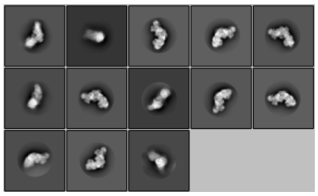

2. 3D classifications

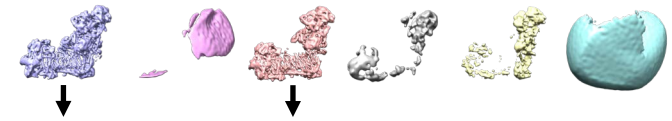

371884 selected particles

3. Refinement, polishing, CTF refinement

Extract at full size, auto-refine	6.1 Å
Ctf refinement, polishing, Ctf refinement	3.8 Å

4. 3D classification without alignment, T8

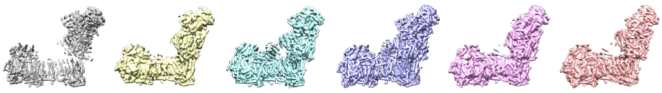

140940 selected particles

Auto-refine – PA mask 3.7 Å

5. Focus-Revert-Classify

3D classification on PA-aligned map, loose membrane arm mask, no searches, T16

Class1 Junk 11.5k p. | Class2 Closed 41.4k p. | Class3 Open 35.9k p. | Class4 Junk 8.4k p. | Class5 Junk 19k p. | Class6 Junk 26.3k p.

Closed
41.4k (53.5%) particles
Entire: 3.9 Å
PA: 3.7 Å,
MA: 3.9 Å

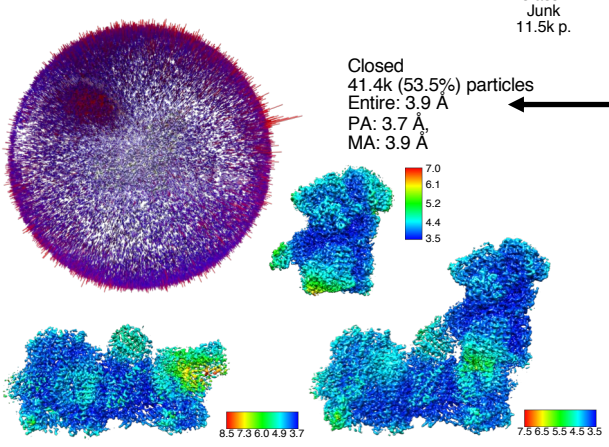

Consensus Open
35.9k (46.5%) particles
Entire: 4.0 Å
PA: 3.8 Å,
MD: 4.0 Å

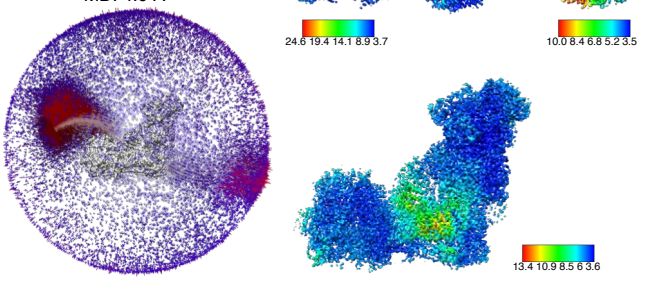

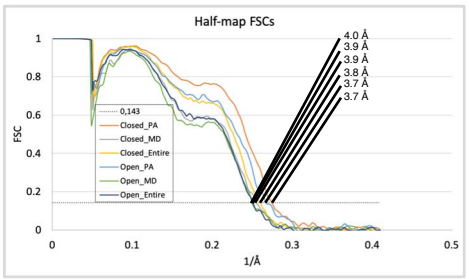

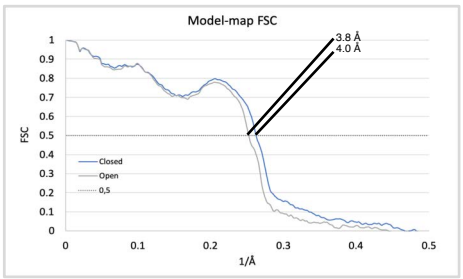

Figure S13

Table S1. Model overview.

Subunit name	Chain	Range built/(out of total) residues	Unmodelled residues	Atomic model (%)	Cofactors	Notes
NuoF	F	1-442/445	443-445	99.3	FMN, NADH N3 (4Fe)	Several conformations
NuoE	E	11-166/166	1-10	93.9	N1a (2Fe)	Several conformations
NuoG	G	4-908/910	1-3, 909-910	99.4	N1b (2Fe) N4 (4Fe) N5 (4Fe) N7 (4Fe) Ca^{2+}	
NuoCD	C	12-600/600	1-11	98.1	DQ	Several conformations
NuoB	B	2-220/220	1, 30-35	97.2	N2 (4Fe)	Several conformations
NuoI	I	1-180/180	-	100	N6a (4Fe) N6b (4Fe)	Several conformations
NuoH	H	3-325/325	1-2	99.3	DQ, Piericidin A	Several conformations
NuoA	A	6-134/147	1-5, 135-147	88.4		Several conformations
NuoJ	J	1-175/184	176-184	95.1		Several conformations
NuoK	K	1-100/100	-	100		
NuoN	N	1-485/485	439-445	98.7		
NuoM	M	1-504/509	505-509	99		
NuoL	L	1-612/613	438-453, 613	97.4		

	DDM_APO	DDM_NADH
	Resting	Resting
Data collection and processing		
Microscope	Titan Krios	Titan Krios
Camera	Falcon 3 linear	Falcon 3 linear
Magnification	75000	75000
Voltage (kV)	300	300
Electron exposure (e/Å2)	89	89
Automation software	EPU	EPU
Number of frames	40	40
Defocus range (μm)	~ -1 to -2	~ -1 to -2
Pixel size (Å)	1.061	1.061
Symmetry imposed	C1	C1
Number of micrographs	3658	3492
Initial particle images	755k	441k
Final particle images	121k	145k
Map resolution (Å) at 0.143 FSC threshold	3.58 Entire 3.18 PA, 3.40 MD	3.22 Entire 2.99 PA, 3.30 MD
Refinement		
Initial model used (PDB code)	3RKO + 4HEA homology models	3RKO + 4HEA homology models
Refinement package	Phenix, real space	Phenix, real space
Model resolution (Å) 0.5 FSC threshold	3.34	3.21
Local resolution range (Å)	3.2-7.0	3.0-6.2
Cross-correlation		
Mask	0.88	0.87
Volume	0.87	0.87
Map sharpening B factor (Å2)	-99 Entire, -81 PA, -100 MD	-82 Entire -76 PA, -85 MD
Model composition		
Protein residues	4675	4681
Ligands	13	15
B factors (Å)		
Protein	87	75
Ligand	104	88
Q-scores		
Protein + ligands	0.60	0.62
R.m.s. deviations		
Bond length (Å)	0.004	0.004
Bond angles (°)	0.821	0.813
Validation		
MolProbity score	1.67	1.66
EMRinger score	2.07	2.36
Clashscore	7.03	7.18
Poor rotamers (%)	0.45	0.29
C-beta deviations (%)	0	0
CaBLAM outliers (%)	1.94	1.99
Ramachandran plot		
Favored (%)	95.94	96.07
Allowed (%)	4.06	3.93
Disallowed (%)	0	0

Table S2. Data processing and refinement statistics, *E. coli* CI.

	DDM/LMNG APO		DDM/LMNG Turnover pH6		
	Resting	Open	Resting	Open	Closed
Data collection and processing					
Microscope	Titan Krios		Titan Krios		
Camera	K3		K3		
Magnification	81000		81000		
Voltage (kV)	300		300		
Electron exposure (e/Å2)	78		78		
Automation software	Serial-EM		Serial-EM		
Number of frames	60		60		
Defocus range (μm)	~ -1 to -2		~ -1 to -2		
Pixel size (Å)	1.06		1.06		
Symmetry imposed	C1		C1		
Number of micrographs	3815		2757		
Initial particle images	918k		773k		
Final particle images	199.3k	167k	92.8k	97.9k	8.2k
Map resolution (Å) at 0.143 FSC threshold	2.7 Entire 2.4 PA, 2.6 MD	2.4 Entire 2.2 PA, 2.4 MD	3.1 Entire 2.6 PA, 2.8 MD	2.5 Entire 2.3 PA, 2.6 MD	3.4 Entire 3.2 NuoFEG, 3.2 NuoN-CD, 3.3 NuoNML
Refinement					
Initial model used (PDB code)	3RKO + 4HEA homology models		3RKO + 4HEA homology models		
Refinement package	Phenix, real space refine		Phenix, real space refine		
Model resolution (Å) 0.5 FSC threshold	2.52	2.5	2.72	2.48	3.34
Local resolution range(Å)	2.3-6.2	2.2-7.0	2.7-6.7	2.2-5.5	3.0-20
Cross-correlation					
Mask	0.9	0.89	0.92	0.92	0.85
Volume	0.9	0.89	0.92	0.91	0.84
Map sharpening B factor (Å2)	-33 Entire, -13 PA, -28 MD	-15 Entire, -9 PA, -17 MD	-50 Entire -18 PA, -20 MD	-19 Entire -8 PA, -20 MD	-29 Entire -10 NuoFEG, 0 NuoN-CD, -10 NuoNML
Model composition					
Protein residues	4612	4717	4645	4732	4772
Ligands	23	25	30	36	25
Waters	Total: 837 PA: 665 MD: 172	Total: 948 PA: 683 MD: 265	Total: 581 PA: 421 MD: 160	Total: 987 PA: 639 MD: 348	-
B factors (Å)					
Protein	57	54	61	54	61
Ligand	85	84	100	93	83
Waters	43	43	42	46	-
Q-scores					
Protein + ligands	0.75	0.74	0.74	0.77	0.62
Water	0.89	0.89	0.90	0.90	-
R.m.s. deviations					
Bond length (Å)	0.004	0.005	0.006	0.005	0.004
Bond angles (°)	0.769	0.803	0.709	0.736	0.754
Validation					
MolProbity score	1.61	1.51	1.57	1.41	1.55
EMRinger score	4.17	4.62	4.49	4.61	3.07
Clashscore	4.94	4.99	4.23	4.47	6.47
Poor rotamers (%)	1.94	1.61	2.11	1.47	0.49
C-beta deviations	0	0.02	0	0	0
CaBLAM outliers (%)	1.18	1.40	1.18	1.18	1.51
Ramachandran plot					
Favored (%)	97.28	97.56	97.41	97.76	96.81
Allowed	2.68	2.4	2.56	2.2	3.17
Disallowed (%)	0.04	0.04	0.02	0.04	0.02

Table S3. Data processing and refinement statistics, *E. coli* CI.

	DDM/LMNG DQ		DDM/LMNG NADH+FMN	DDM/LMNG PiericidinA + FMN
	Resting	Open	Open	Open
Data collection and processing				
Microscope	Titan Krios		Titan Krios	Glacios
Camera	K3		K3	Falcon3
Magnification	81000		81000	120000
Voltage (kV)	300		300	200
Electron exposure (e/Å2)	78		78	90
Automation software	Serial-EM		Serial-EM	EPU
Number of frames	60		60	65
Defocus range (μm)	~ -1 to -2		~ -1 to -2	~ -1.2 to -2.4
Pixel size (Å)	1.06		1.06	1.21
Symmetry imposed	C1		C1	C1
Number of micrographs	3150		3033	3582
Initial particle images	852k		563k	463k
Final particle images	66.8k	56.2k	36.8k	99.9k
Map resolution (Å) at 0.143 FSC threshold	3.1 Entire 2.6 PA, 2.8 MD	2.7 Entire 2.5 PA, 2.8 MD	3.0 Entire 2.8 PA, 3.0 MD	3.2 Entire 3.0 PA, 3.2 MD
Refinement				
Initial model used (PDB code)	3RKO + 4HEA homology models		3RKO + 4HEA homology models	
Refinement package	Phenix, real space refine		Phenix, real space refine	
Model resolution (Å) 0.5 FSC threshold	2.88	2.81	3.0	3.21
Local resolution range(Å)	2.6-8.3	2.3-7.4	2.7-8.6	2.8-8.8
Cross-correlation				
Mask	0.88	0.9	0.88	0.88
Volume	0.89	0.9	0.89	0.88
Map sharpening B factor (Å2)	-33 Entire, -17 PA, -24 MD	-20 Entire, -11 PA, -21 MD	-29 Entire -21 PA, -24 MD	-65 Entire -62 PA, -64 MD
Model composition				
Protein residues	4630	4719	4710	4720
Ligands	23	28	32	26
B factors (Å)				
Protein	70	62	73	86
Ligand	102	92	109	110
Q-scores				
Protein + Ligand	0.68	0.71	0.65	0.61
R.m.s. deviations				
Bond length (Å)	0.006	0.005	0.005	0.004
Bond angles (°)	0.7	0.756	0.769	0.739
Validation				
MolProbity score	1.63	1.43	1.52	1.36
EMRinger score	3.63	4.09	3.47	2.89
Clashscore	4.97	4.92	6.11	5.31
Poor rotamers (%)	2.21	1.25	1.3	0.39
C-beta deviations	0	0	0	0
CaBLAM outliers (%)	1.19	1.38	1.41	1.51
Ramachandran plot				
Favored (%)	97.47	97.54	97.51	97.63
Allowed (%)	2.51	2.44	2.46	2.35
Disallowed (%)	0.02	0.02	0.02	0.02

Table S4. Data processing and refinement statistics, *E. coli* CI.

	DDM/LMNG Turnover pH8			
	Resting	Open	Open-ready	Closed
Data collection and processing				
Microscope	Titan Krios			
Camera	K3			
Magnification	81000			
Voltage (kV)	300			
Electron exposure (e/Å2)	80			
Automation software	Serial-EM			
Number of frames	80			
Defocus range (μm)	~ -1 to -2			
Pixel size (Å)	1.06			
Symmetry imposed	C1			
Number of micrographs	8659			
Initial particle images	1.65M			
Final particle images	82.6k	67.2k	40.8k	32.6k
Map resolution (Å) at 0.143 FSC threshold	3.1 Entire 2.6 PA, 3.1 MD	3.0 Entire 2.6 PA, 3.1 MD	3.0 Entire 2.7 PA, 3.0 MD	3.0 Entire 2.7 PA, 3.1 MD
Refinement				
Initial model used (PDB code)	3RKO + 4HEA homology models			
Refinement package	Phenix, real space refine			
Model resolution (Å) 0.5 FSC threshold	3.0	3.0	3.0	3.0
Local resolution range(Å)	2.6-8.3	2.3-7.4	2.7-8.6	2.8-8.8
Cross-correlation				
Mask	0.87	0.88	0.88	0.87
Volume	0.86	0.87	0.88	0.87
Map sharpening B factor (Å2)	-34 Entire, -25 PA, -38 MD	-30 Entire, -19 PA, -34 MD	-28 Entire -22 PA, -33 MD	-23 Entire -20 PA, -27 MD
Model composition				
Protein residues	4645	4732	4751	4764
Ligands	23	25	26	28
B factors (Å)				
Protein	66	62	52	61
Ligand	93	88	83	82
Q-scores				
Protein + Ligand	0.67	0.68	0.70	0.69
R.m.s. deviations				
Bond length (Å)	0.007	0.004	0.004	0.004
Bond angles (°)	0.848	0.77	0.747	0.776
Validation				
MolProbity score	1.68	1.7	1.47	1.65
EMRinger score	3.49	2.92	3.18	2.63
Clashscore	5.41	5.58	5.5	5.73
Poor rotamers (%)	1.96	2.59	1.65	2.08
C-beta deviations	0	0	0	0
CaBLAM outliers (%)	1.32	1.29	1.35	1.65
Ramachandran plot				
Favored (%)	97.02	97.59	97.98	97.53
Allowed (%)	2.96	2.39	2.0	2.45
Disallowed (%)	0.02	0.02	0.02	0.02

Table S5. Data processing and refinement statistics, *E. coli* CI.

	LMNG APO	LMNG Turnover pH6			
	Open-ready	Resting	Open	Open-ready	Closed
Data collection and processing					
Microscope	Glacios	Titan Krios			
Camera	Falcon3	K3			
Magnification	120000	81000			
Voltage (kV)	200	300			
Electron exposure (e/Å2)	74	80			
Automation software	EPU	Serial-EM			
Number of frames	53	80			
Defocus range (μm)	~ -1.2 to -2.4	~ -1 to -2			
Pixel size (Å)	1.21	1.06			
Symmetry imposed	C1	C1			
Number of micrographs	4295	11316			
Initial particle images	1M	4.5M			
Final particle images	109k	189.7k	31.8k	317.1k	170k
Map resolution (Å) at 0.143 FSC threshold	3.4 Entire 3.2 NuoFEG, 3.3 NuoN-CD, 3.4 NuoNML	2.7 Entire 2.4 PA, 2.95 MD	3.1 Entire 2.88 PA, 3.14 MD	2.35 Entire 2.15 PA, 2.38 MD	2.5 Entire 2.3 PA, 2.5 MD
Refinement					
Initial model used (PDB code)	3RKO + 4HEA homology models				
Refinement package	Phenix, real space refine				
Model resolution (Å) 0.5 FSC threshold	3.5	2.61	3.5	2.12	2.27
Local resolution range(Å)	3.0-11.2	2.2-10.8	2.7-13.7	2.2-5.5	2.2-5.8
Cross-correlation					
Mask	0.85	0.89	0.87	0.93	0.92
Volume	0.84	0.89	0.86	0.93	0.92
Map sharpening B factor (Å2)	-70 Entire -50 NuoFEG, -50 NuoN-CD, -60 NuoNML	-26 Entire, -18 PA, -39 MD	-32 Entire -24 PA, -35 MD	-16 Entire -13 PA, -22 MD	-15 Entire -12 PA, -25 MD
Model composition					
Protein residues	4750	4650	4721	4748	4774
Ligands	14	28	23	28	25
Waters				Total: 1298 PA: 865 MD: 433	Total: 1184 PA: 850 MD: 334
B factors (Å)					
Protein	92	57	61	43	48
Ligand	95	94	100	67	71
Waters	-	-	-	40	41
Q-scores					
Protein + ligands	0.57	0.74	0.67	0.82	0.80
Water	-	-	-	0.93	0.92
R.m.s. deviations					
Bond length (Å)	0.004	0.006	0.005	0.005	0.006
Bond angles (°)	0.849	0.815	0.746	0.735	0.794
Validation					
MolProbity score	1.51	1.56	1.37	1.44	1.45
EMRinger score	2.15	3.87	2.91	5.2	4.92
Clashscore	6.72	4.84	5.86	4.62	4.21
Poor rotamers (%)	0.41	1.56	0.23	1.68	1.67
C-beta deviations	0	0	0	0	0
CaBLAM outliers (%)	1.46	1.18	1.27	1.35	1.27
Ramachandran plot					
Favored (%)	97.26	97.39	97.78	97.86	97.66
Allowed	2.72	2.56	2.16	2.1	2.26
Disallowed (%)	0.02	0.04	0.02	0.04	0.08

Table S6. Data processing and refinement statistics, *E. coli* CI.

	Ovine CxI pH5.5		Ovine CxI pH7.4		Ovine CxI pH9	
	Closed	Open	Closed	Open	Closed	Open
Data collection and processing						
Microscope	Glacios		Glacios		Glacios	
Camera	Falcon 3EC		Falcon 3EC		Falcon 3EC	
Magnification	120000		120000		120000	
Voltage (kV)	200		200		200	
Electron exposure (e/Å2)	90		90		90	
Automation software	EPU		EPU		EPU	
Number of frames	65		65		59	
Defocus range (μm)	~ -1 to -2		~ -1 to -2		~ -1 to -2	
Pixel size (Å)	1.22		1.22		1.22	
Symmetry imposed	C1		C1		C1	
Number of micrographs	2097		2931		2799	
Initial particle images	557.7k		557.6k		660.5k	
Final particle images	32.9k	97.6k	50.8k	113.7k	41.4k	35.9k
Map resolution (Å) at 0.143 FSC threshold	3.5 Entire 3.4 PA, 3.5 MD	3.3 Entire 3.2 PA, 3.3 MD	3.5 Entire 3.4 PA, 3.5 MD	3.2 Entire 3.1 PA, 3.2 MD	3.9 Entire 3.7 PA, 3.9 MD	3.9 Entire 3.7 PA, 4.0 MD
Refinement						
Initial model used (PDB code)	6ZKC	6ZKE	6ZKC	6ZKE	6ZKC	6ZKE
Refinement package	Phenix, real space refine		Phenix, real space refine		Phenix, real space refine	
Model resolution (Å) 0.5 FSC threshold	3.5	3.3	3.5	3.2	3.8	3.9
Local resolution range(Å)	3.2-7.9	3.0-5.7	3.2-6.6	2.9-5.0	3.5-8.7	3.6-13.4
Cross-correlation						
Mask	0.89	0.9	0.89	0.9	0.84	0.85
Volume	0.89	0.89	0.89	0.89	0.84	0.84
Map sharpening B factor (Å2)	-61 Entire, -71 PA, -78 MD	-60 Entire, -62 PA, -67 MD	-59 Entire, -60 PA, -78 MD	-63 Entire, -72 PA, -72 MD	-92 Entire, -83 PA, -107 MD	-87 Entire, -74 PA, -109 MD
Model composition						
Protein residues	8227	8153	8227	8160	8195	8160
Ligands	32	16	43	46	22	17
B factors (Å)						
Protein	55.5	62.5	61.9	56.2	71.1	77.4
Ligand	87	80	95.4	88.4	102.8	100.3
Q-scores						
Protein + Ligand	0.61	0.64	0.59	0.64	0.52	0.51
R.m.s. deviations						
Bond length (Å)	0.005	0.004	0.004	0.005	0.004	0.004
Bond angles (°)	0.81	0.73	0.72	0.75	0.81	0.8
Validation						
MolProbity score	1.54	1.37	1.45	1.41	1.58	1.52
EMRinger score	2.24	2.69	2.07	2.61	1.55	1.51
Clashscore	5.28	4.37	4.88	4.41	5.9	5.92
Poor rotamers (%)	0.36	0.31	0.28	0.24	0.42	0.22
C-beta deviations	0.01	0	0	0	0	0
CaBLAM outliers (%)	1.59	1.3	1.4	1.3	1.58	1.3
Ramachandran plot						
Favored (%)	96.26	97.13	96.87	96.88	96.21	96.85
Allowed (%)	3.72	2.86	3.11	3.12	3.77	3.15
Disallowed (%)	0.02	0.01	0.01	0.00	0.01	0.00

Table S7. Data processing and refinement statistics, ovine CI.

Table S8. Mutations in the *E. coli* complex I and their structural context.

Oxidoreductase activities were measured with either O_2, DQ or UQ_1 as final acceptor and the range observed is shown. FMN-site activities were measured with either ferricyanide or hexaammineruthenium III as final acceptor. Proton pumping rates are very approximate. "Reduced" corresponds to the value ~50-80% and "low" to below ~50%. Abbreviations: SB - salt bridge, HB – hydrogen bond, HL – helix HL.

a) Mutations in the peripheral arm

Mutation	Amino acid location	Expression/ assembly	Effect			Reference and comments
			FMN-site activity	Oxido-reductase activity	Proton pumping activity	
NuoF						
E95Q	NADH site	normal	20-40%	40%	NA	(*1*)
NuoCD						
S104A	surface	NA	103%	106-114%	NA	(*2*)
A134S	surface	NA	82%	NA	NA	(*2*)
E138A	Intersubunit interface, before $_{CD}$LHL	low	49%	2-3%	0%	(*2*)
E138Q		normal	44%	20-29%	40%	(*2*)
E138D		reduced	51%	4-6%	10%	(*2*)
R139A		NA	87%	102-118%	NA	(*2*)
E140A		reduced	42%	5-7%	0%	(*2*)
E140Q		reduced	33%	7-11%	0%	(*2*)
E140D		normal	94%	85-104%	100%	(*2*)
D143A		reduced	50%	2-3%	0%	(*2*)
D143N		reduced	69%	5-9%	10%	(*2*)
D143E		normal	103%	128-132%	90%	(*2*)
G146A	surface	NA	102%	114-117%	NA	(*2*)
F149A		NA	109%	NA	NA	(*2*)
R156A		NA	124%	123-131%	NA	(*2*)
G166A		NA	113%	117%	NA	(*2*)
H167A		NA	93%	74-97%	NA	(*2*)
P168A	$_{CD}$LHL	NA	91%	75-84%	NA	(*2*)
K171A		NA	76%	71-80%	NA	(*2*)
K171R		NA	80%	78-88%	NA	(*2*)
P182A		NA	100%	71-88%	NA	(*2*)
G221V	NuoCD loop, Q site	NA	50%	1-6%	NA	(*3*)
P222A		reduced	51%	7-9%	NA	(*3*)
H224A		NA	88%	64%	65%	(*4*)
H228A		NA	100%	48%	50%	(*4*)
H228R		normal	85%	67-98%	NA	(*3*)
G229A		normal	67%	24-38%	NA	(*3*)
G229V		reduced	42%	1-4%	NA	(*3*)
R232A		NA	76%	50-74%	NA	(*3*)
R232K		NA	80%	61-93%	NA	(*3*)
G239A	NuoA loop interface	normal	96%	88-118%	NA	(*3*)
G239V		reduced	62%	35-52%	NA	(*3*)
E240A	NuoH interface	normal	103%	14-26%	NA	(*3*)

a) Mutations in the peripheral arm, continuation

Mutation	Amino acid location	Expression/ assembly	Effect			Reference and comments
			FMN-site activity	Oxido-reductase activity	Proton pumping activity	
NuoCD						
E240D	NuoH interface	normal	71%	46-75%	NA	(*3*)
H253A	N2 environment	low	24%	13-18%	NA	(*3*)
H253K		low	26%	4-7%	NA	(*4*)
G255A		normal	81%	82-105%	NA	(*3*)
G255V		reduced	67%	35-51%	NA	(*3*)
R274A		normal	47%	3-4%	NA	(*3*)
R274K		normal	77%	45-60%	NA	(*3*)
R274A		NA	77%	22%	25%	(*4*)
Y277A	N2 environment, Q site	normal	66%	3-7%	NA	(*3*)
Y277W		normal	60%	2-8%	NA	(*3*)
Y277F		NA	76%	17-27%	NA	(*3*), capsaicin-40 insensitive
E292Q	Intersubunit interface, SB with $_{C}$R307	low	29%	4-6%	NA	(*3*)
E292D		low	14%	2-8%	NA	(*3*)
R302A	surface	normal	78%	78-97%	NA	(*3*)
R302K		normal	94%	92-105%	NA	(*3*)
E312Q	Intersubunit interface SB with cR439	low	19%	3-7%	NA	(*3*)
E312D		normal	82%	80-95%	NA	(*3*)
R315A	Intersubunit interface	low	30%	2-3%	NA	(*3*)
R315K		reduced	49%	41-49%	NA	(*3*)
H319A	Intersubunit interface	normal	82%	84-106%	NA	(*3*)
H319R		normal	47%	30-38%	NA	(*3*)
D329A	Q-site, HB with $_{C}$H228	normal	92%	42-56%	NA	(*3*)
D329E		normal	87%	54-63%	NA	(*3*)
H359A	HB with N2	reduced	74%	13-28%	NA	(*3*)
H359K		reduced	68%	36-52%	NA	(*3*)
R560K	Part of internal β-sheet	low	40%	8-14%	NA	(*3*)
R600A	Intersubunit interface	reduced	61%	47-56%	NA	(*3*)
NuoB						
E67Q	Close to N2, HB with $_{C}$R357	NA	89%	10%	NA	(*5*), piericidin A insensitive
E67D		NA	100%	78%	NA	(*5*), piericidin A insensitive
D77N	NuoH interface, part of Q-cavity	NA	78%	12%	NA	(*5*), piericidin A insensitive
D77E		NA	78%	54%	NA	(*5*)
D94N	NuoH interface, part of Q-cavity	NA	78%	12%	NA	(*5*)
D94E		NA	89%	83%	NA	(*5*)
Y114C	Intersubunit interface	normal	80%	100%	NA	(*6*)
D115N		NA	78%	45%	NA	(*5*)
Y114C/ Y139F		normal	50%	20%	NA	(*6*)
E119Q	Intersubunit interface	NA	78%	88%	NA	(*5*)
Y139C	cdLHL interface	normal	80%	100%	NA	(*6*)
D146N	NuoI interface	NA	89%	59%	NA	(*5*)
D152N	surface	NA	78%	59%	NA	(*5*)

Y154H	Part of internal β-sheet	normal	90%	100%	NA	(*6*)
E163Q	HB with $_{B}$R161	NA	78%	76%	NA	(*5*)

a) Mutations in the peripheral arm, continuation

Mutation	Amino acid location	Expression/ assembly	Effect			Reference and comments
			FMN-site activity	Oxido-reductase activity	Proton pumping activity	
NuoI						
C60A	Bond with N6a Fe-S cluster	NA	17%	1-2%	0%	(*7*)
C60S		NA	31%	5-7%	5%	(*7*)
C60H		NA	20%	2%	0%	(*7*)
C63A		NA	23%	2%	0%	(*7*)
C63S		normal	50%	20%	20%	(*7*)
C66S		NA	18%	22%	0%	(*7*)
C66H		NA	19%	1-2%	0%	(*7*)
C70S	Bond with N6b Fe-S cluster	NA	19%	4%	0%	(*7*)
C70H		NA	15%	1-2%	0-5%	(*7*)
C99S		NA	17%	1-2%	0%	(*7*)
C99H		NA	15%	1%	0%	(*7*)
C102S		NA	15%	2-5%	0-5%	(*7*)
C102H		NA	17%	1-2%	0%	(*7*)
C105S		NA	17%	1-2%	0%	(*7*)
C109S		NA	21%	1-4%	0%	(*7*)
T30A	NuoH interface	NA	64%	58-61%	reduced	(*7*)
P34A	H1 connecting loop	NA	65%	57-65%	reduced	(*7*)
P42A	NuoCD interface	NA	108%	61-65%	reduced	(*7*)
R43A		NA	84%	46-53%	reduced	(*7*)
Y44A	NuoB interface	NA	139%	120%	100%	(*7*)
G46A	Close to N6b	NA	79%	78%	100%	(*7*)
R52A	Surface, part of N6a interacting loop	NA	84%	64-75%	100%	(*7*)
P54A		NA	95%	73-79%	100%	(*7*)
G56A		NA	94%	47-54%	reduced	(*7*)
E58A		NA	99%	64-85%	reduced	(*7*)
V61A		normal	67%	31-33%	reduced	(*7*)
L65A	Close to N6a	normal	74%	67-72%	70%	(*7*)
P71A	N6b interface	normal	75%	45-56%	reduced	(*7*)
I75A		normal	66%	28-40%	reduced	(*7*)
G85A	surface	NA	106%	88-116%	100%	(*7*)
F92A	N6a interface	NA	79%	76-81%	100%	(*7*)
R93A	surface	NA	101%	92-101%	100%	(*7*)
I94A	Nba interface	normal	108%	92-99%	100%	(*7*)
I94G		NA	92%	93-119%	NA	(*7*)
R98A	Intersubunit interface, near $_{B}$C99	normal	53%	9-18%	20%	(*7*)
I100A		normal	101%	85-86%	NA	(*7*)
I100G		NA	86%	61-85%	NA	(*7*)
G103A	near N6b	NA	88%	80-100%	100%	(*7*)
E107A	NuoCD interface,	normal	67%	58-71%	reduced	(*7*)
P110A	N6a interface	normal	78%	9-19%	reduced	(*7*)
I114A	near N6a and N6b	NA	94%	107-121%	100%	(*7*)
E121A	surface	normal	99%	74-85%	80%	(*7*)
Y132A	surface	NA	123%	84-105%	100%	(*7*)

b) Mutations in the membrane arm

Mutation	Amino acid location	Expression/ assembly	Effect			Reference and comments
			FMN-site activity	Oxido-reductase activity	Proton pumping activity	
NuoL						
D82A	β-hairpin - TM8 SB	normal	90%	90%	80%	(*8*)
D82N		normal	90%	75%	80%	(*8*)
D134N	surface, interacts with β-hairpin	normal	110%	110%	70%	(*8*)
E144A	TM5, central axis, interface with NuoM	reduced	90%	20%	30%	(*8*)
E144Q		normal	105%	15%	10%	(*8*)
K169C	TM6 – HL SB	normal	87%	65%	reduced	(*9*)
K169E		normal	117%	67%	reduced	(*9*)
K169R		normal	118%	94%	reduced	(*9*)
D178A	TM6, central axis	normal	125%	95%	80%	(*8*)
D178N		normal	125%	70%	50%	(*8*), (EIPA insensitive)
R175A	NuoL/M interface	reduced	60%	17%	low	(*10*), (EIPA insensitive)
K229A	TM7, central axis	low	60%	10%	NA	(*8*)
K229R		normal	125%	30%	NA	(*8*)
K229E		low	100%	20%	NA	(*8*)
P234A	Intramembrane surface	reduced	85%	67%	reduced	(*10*)
Q236H	TM7b – HL HB	normal	108%	86%	NA	(*9*)
Q236K		normal	99%	57%	low	(*9*)
Q236C		normal	106%	86%	NA	(*9*)
Q236E		normal	117%	84%	NA	(*9*)
W238A	TM7b - TM7a HB	normal	130%	80%	NA	(*8*)
W238Y		low	100%	50%	NA	(*8*)
W238C		low	90%	30%	NA	(*8*)
D303A	surface, interacts with TM11-12 loop	normal	110%	110%	80%	(*8*), (EIPA insensitive)
D303N		normal	115%	100%	80%	(*8*)
H334A	central axis, proton channel	low	100%	50%	NA	(*8*)
H334Q		normal	150%	120%	NA	(*8*)
H338A		normal	110%	100%	NA	(*8*)
H338Q		normal	100%	100%	NA	(*8*)
K342A	central axis, proton channel	low	63%	11%	low	(*10*)
E359A	surface	normal	110%	100%	normal	(*8*)
P390A	Intramembrane surface	reduced	90%	68%	NA	(*10*)
K399A	central axis, proton channel	low	105%	20%	NA	(*8*)
K399E		low	100%	15%	NA	(*8*)
D400A	central axis, proton channel, surface	normal	120%	70%	50%	(*8*), (EIPA insensitive)
D400N		normal	105%	90%	70%	(*8*)
D400E		normal	130%	100%	90%	(*8*)
R431A	surface, near HL	low	60%	10%	NA	(*8*)
R431H		normal	120%	100%	NA	(*8*)

b) Mutations in the membrane arm, continuation

Mutation	Amino acid location	Expression/ assembly	Effect			Reference and comments
			FMN-site activity	Oxido-reductase activity	Proton pumping activity	
NuoL						
R529C	Horizontal amphipathic helix HL	NA	NA	86%	NA	(*11*)
D542R		NA	61%	64%	102%	(*12*)
D542N		NA	78%	91%	105%	(*12*)
D542N		NA	NA	81%	77%	(*13*)
D546N		NA	NA	93%	90%	(*13*)
K551C		NA	NA	100%	NA	(*11*)
K551Q		NA	89%	104%	96%	(*12*)
K551E		NA	80%	98%	96%	(*12*)
V550C		NA	NA	74%	NA	(*11*)
P552A		NA	100%	121%	109%	(*12*)
P552C		NA	88%	108%	103%	(*12*)
P552Q		NA	96%	120%	98%	(*12*)
F553C		NA	NA	104%	NA	(*11*)
L554C		NA	NA	93%	NA	(*11*)
L560C		NA	NA	50%	NA	(*11*)
K561C		NA	NA	97%	NA	(*11*)
R562C		NA	NA	81%	NA	(*11*)
D563N		NA	NA	75%	49%	(*13*)
D563E		NA	NA	106%	74%	(*13*)
D563Q		NA	NA	81%	56%	(*13*)
D563A		NA	NA	118%	82%	(*13*)
N566C		NA	NA	69%	NA	(*11*)
I571C		NA	NA	80%	NA	(*11*)
P572C		NA	NA	119%	NA	(*11*)
A573C		NA	NA	102%	NA	(*11*)
V574C		NA	NA	86%	NA	(*11*)
Y590C		NA	NA	102%	NA	(*11*)
NuoM						
D84A	β-hairpin - TM8 SB	normal	92%	83%	NA	(*14*)
D84N		normal	97%	89%	NA	(*14*)
D135A	surface, interacts with β -hairpin	reduced	80%	44%	normal	(*14*)
D135N		normal	86%	78%	normal	(*14*)
D135E		normal	93%	87%	normal	(*14*)
E144A	TM5, central axis, interface with NuoN	normal	103%	2-10%	0%	(*14*)
E144Q		normal	98%	2%	0%	(*14*)
E144D		normal	100%	89-100%	normal	(*14*)
E144A/M 145E		normal	86%	3-10%	0%	(*15*)
E144A/W 143E		normal	91%	13-15%	15%	(*15*)

b) Mutations in the membrane arm, continuation

Mutation	Amino acid location	Expression/assembly	Effect			Reference and comments
			FMN-site activity	Oxido-reductase activity	Proton pumping activity	
NuoM						
E144A/V148E	TM5, central axis, interface with NuoN	normal	113%	3-12%	0%	(*15*)
E144A/F140E		normal	88%	39-60%	60%	(*15*)
E144A/F152E		normal	85%	3-11%	0%	(*15*)
E144A/F141E		normal	99%	3-15%	0%	(*15*)
E144A/L147E		normal	95%	30-45%	50%	(*15*)
E144A/F139E		normal	104%	2-15%	0%	(*15*)
E144A/F142E		normal	103%	3-15%	0%	(*15*)
E144A/M146E		normal	86%	2-11%	0%	(*15*)
E144A/P149E		normal	88%	4-10%	0%	(*15*)
E144A/M150E		normal	93%	2-12%	0%	(*15*)
E144A/Y151E		normal	98%	3-10%	0%	(*15*)
E144A/L153E		normal	91%	3-13%	0%	(*15*)
E144A/V127E		normal	95%	3%	0%	(*15*)
E144A/I128E		normal	109%	3-13%	0%	(*15*)
E144A/G129E		normal	85%	5-12%	0%	(*15*)
E144A/I189E		normal	111%	3-13%	0%	(*15*)
E144A/L190E		normal	98%	2-12%	0%	(*15*)
E144A/A191E		normal	85%	3-12%	0%	(*15*)
K173C	TM6 – HL HB	normal	78%	70%	reduced	(*9*)
K173E		normal	102%	50%	reduced	(*9*)
K173R		normal	94%	91%	reduced	(*9*)
H196A	surface	normal	99%	79%	NA	(*14*)
K234A	TM7, central axis	normal	91%	5-10%	low	(*14*)
K234R		reduced	65%	5-20%	low	(*16*)
H241A	TM7b - HL interaction	normal	90%	88%	NA	(*14*)
H241E		normal	79%	71%	NA	(*9*)
H241K		normal	94%	40%	low	(*9*)
H241R		normal	81%	46%	NA	(*9*)
W243A	TM7b – TM7a HB	normal	97%	103%	normal	(*14*)
W243Y		normal	108%	104%	NA	(*14*)
P245A	TM7b surface	normal	100%	102%	NA	(*14*)
K265A	TM8, central axis	normal	96%	35-80%	low	(*14*)
R273A	TM8 - β-hairpin SB	normal	105%	92%	NA	(*14*)
H322A	central axis	normal	99%	100%	NA	(*14*)
H322A		NA	NA	61%	74-92%	(*17*)
H348A	central axis	normal	100%	92%	NA	(*14*)
H348A		NA	NA	82%	61-79%	(*17*)
H322/H348		NA	NA	48	40-63%	(*17*)
R365A	surface, SB TM11-TM14	normal	85%	87%	NA	(*14*)
R369H	surface, HB to TM7b	normal	94%	63-68%	normal	(*14*)
P399A	Broken helix at M/L interface	normal	78%	52-63%	reduced	(*10*)
E407A	TM12, NuoL interface, central axis	normal	65%	5-8%	low	(*10*)
Y435A	proton channel	normal	99%	94	NA	(*14*)

b) Mutations in the membrane arm, continuation

Mutation	Amino acid location	Expression/ assembly	Effect			Reference and comments
			FMN-site activity	Oxido-reductase activity	Proton pumping activity	
NuoN						
M74K	surface	normal	NA	90%	100%	(*18*)
C88S	TM3, interior	normal	NA	100%	100%	(*18*)
C88V		normal	NA	100%	100%	(*18*)
E104C	surface, near NuoJ	normal	NA	90%	100%	(*18*)
E133A	TM5, central axis / interface with NuoK	normal	NA	70%	100%	(*18*)
E133C		normal	NA	70%	100%	(*18*)
E133D		normal	NA	80%	100%	(*18*)
E133A		normal	102%	88%	100%	(*10*)
E133A/ $_{K}$E72A		normal	71%	19%	low	(*10*)
R151C	surface	normal	NA	90%	100%	(*18*)
E154C	surface, interacts with NuoK N-terminus	normal	NA	70%	90%	(*18*)
K158C	TM6 – HL HB	normal	86%	50%	80%	(*9*)
K158R		normal	71%	70%	80%	(*9*)
K158E		normal	95%	47%	reduced	(*9*)
K158A		normal	79	57	90%%	(*10*)
K158R		normal	75	41	reduced	(*10*)
T160I	interface with NuoK	normal	NA	80%	NA	(*18*)
K217C	TM7, central axis	No expression	NA	NA	NA	(*18*)
K217R		normal	NA	40%	80%	(*18*)
K217A		normal	92	55%	reduced	(*10*)
K217C		NA	102	57	100%	(*10*)
K217R		normal	87	44	reduced	(*10*)
P222A	loop breaking TM7	normal	91	77	90%	(*10*)
H224A	TM7b - HL interaction	normal	NA	100%	NA	(*18*)
H224A		normal	90	73	80%	(*10*)
H224Y		normal	NA	90%	NA	(*18*)
H224K		normal	95	37-40%	reduced	(*9*, *18*)
H224E		normal	100%	67%	NA	(*9*)
H224R		normal	69%	32%	NA	(*9*)
W226C	TM7b – TM7a HB	normal	NA	90%	100%	(*18*)
D229C	TM7b – $_{L}$TM16 and HL interaction	normal	NA	70%	100%	(*18*)
K247C	TM8, central axis	normal	NA	0-7%	50%	(*18*)
K247R		normal	NA	80%	100%	(*18*)
K247R		NA	101%	94%	normal	(*10*)
K247A		NA	70%	32%	reduced	(*10*)
K295C	surface	normal	NA	80%	70%	(*18*)
K295R		normal	NA	90%	80%	(*18*)
Y300C	TM10 - HL interaction	normal	NA	70%	80%	(*18*)
Y300S		normal	NA	50%	80%	(*18*)

b) Mutations in the membrane arm, continuation

Mutation	Amino acid location	Expression/assembly	Effect			Reference and comments
			FMN-site activity	Oxido-reductase activity	Proton pumping activity	
NuoN						
P387A	TM12 intramembrane loop	normal	83%	52%	reduced	(*10*)
P387G		NA	103%	91%	90%	(*10*)
G391S	near central axis	normal	NA	90%	NA	(*18*)
K395C	TM12, central axis, NuoM interface	normal	NA	5%	NA	(*18*)
K395R		normal	NA	30%	NA	(*18*)
K395R		NA	90%	37%	reduced	(*10*)
K395A		normal	71%	4%	low	(*10*)
Y424C	Facing into proton channel	normal	NA	90%	NA	(*18*)
V469A	Intramembrane surface	normal	88%	72%	90%	(*10*)
M482C	Surface/ N/M interface	normal	NA	100%	NA	(*18*)
NuoK						
F15A	interface with NuoN	normal	102%	90%	NA	(*19*)
G21V	interface with NuoJ	normal	99%	61%	NA	(*19*)
R25A	HBs to backbone of $_{J}$TM1 C-terminus	normal	101%	26%	30%	(*19*)
R25A		reduced	85%	54-73%	70%	(*20*)
R25K		normal	97%	28-31%	NA	(*19*)
R25K		reduced	97%	58-78%	100%	(*20*)
R25C		reduced	97%	53-81%	90%	(*20*)
R25S		reduced	915	51-64%	70%	(*20*)
R26A	surface, near $_{L}$TM16	normal	91%	39%	40%	(*19*)
R26A		reduced	98%	55-73%	90%	(*20*)
R26K		normal	96%	100%	NA	(*19*)
R26K		normal	106%	80-95%	100%	(*20*)
R25A/R26A		normal	90%	14%	30%	(*19*)
N27C	surface, near $_{L}$TM16	normal	95%	67-82%	70%	(*20*)
N27S		normal	75%	59-67%	70%	(*20*)
E36A	E-channel, central axis, interface with NuoJ	normal	95%	1-7%	NA	(*19*)
E36A		normal	86%	3-7%	0%	(*20*)
E36A/M31E		normal	94%	3-5%	0%	(*20*)
E36A/L32E		normal	101%	52-56%	70%	(*20*)
E36A/I33E		normal	85%	2-4%	0%	(*20*)
E36A/G34E		normal	94%	2-3%	0%	(*20*)
E36A/L35E		normal	80%	2-7%	0%	(*20*)
E36A/I37E		normal	98%	3-8%	0%	(*20*)
E36A/M38E		normal	87%	65-69%	90%	(*20*)
E36A/I39E		normal	101%	49-75%	70%	(*20*)
E36A/N40E		normal	78%	47-77%	65%	(*20*)
E36A/A41E		normal	79%	3-4%	0%	(*20*)
E36Q		normal	99%	3-8%	0%	(*19*, *21*)
E36D		normal	118%	120%	normal	(*21*)
E36Q/E72Q		normal	64%	5%	impaired	(*21*)
E36Q/I39D		normal	76%	21%	impaired	(*21*)
E36Q/A69D		normal	52%	91%	normal	(*21*)

b) Mutations in the membrane arm, continuation

Mutation	Amino acid location	Expression/assembly	Effect			Reference and comments
			FMN-site activity	Oxido-reductase activity	Proton pumping activity	
NuoK						
I39D	interface with NuoN	normal	84%	140%	normal	(*21*)
A69D	opposite E36	normal	60%	119%	normal	(*21*)
E72A	E-channel, central axis, interface with NuoN	normal	103%	43-48%	~50%	(*19*)
E72Q		normal	99%	22-77%	~20%	(*19*, *21*)
E72D		normal	76%	100%	normal	(*21*)
E72Q/I39D		normal	54%	180%	normal	(*21*)
E72Q/A69D		normal	92%	77%	impaired	(*21*)
E72Q/G34D		normal	60%	77%	impaired	(*21*)
E36Q/I39D A69D/E72Q		normal	118%	200%	impaired	(*21*)
E72A		normal	105%	47-52%	70%	(*20*)
E72A/S67E		reduced	94%	11-16%	5%	(*20*)
E72A/L68E		normal	84%	57-73%	70%	(*20*)
E72A/A69E		normal	114%	63-74%	90%	(*20*)
E72A/A71E		normal	94%	23-30%	30%	(*20*)
E72A/A73E		normal	77%	28-39%	60%	(*20*)
E72A/I75E		reduced	99%	54-62%	70%	(*20*)
E72A/G75E		normal	106%	68-84%	100%	(*20*)
E72A/L77E		normal	93%	45-55%	50%	(*20*)
R85A	surface	normal	104%	100%	NA	(*19*)
R85K		normal	103%	98%	NA	(*19*)
R87A	surface	normal	103%	99%	NA	(*19*)
R87K		normal	106%	100%	NA	(*19*)
NuoA						
K46A	TM1-TM2 loop, SB to $_H$E71 in closed state	normal	100%	94-100%	NA	(*22*)
E51A	TM1-TM2 loop, SB to $_H$K140 in closed state	normal	97%	30%	NA	(*22*)
D79A	interface between $_J$TM3 and NuoH, central axis	normal	102%	86-95%	NA	(*22*)
D79N		normal	99%	37-44%	NA	(*22*)
E81A	interface with NuoJ	normal	96%	36-42%	NA	(*22*)
E81Q		normal	94%	50-77%	NA	(*22*)
D79N/E81Q		normal	98%	2-10%	NA	(*22*)
NuoJ						
Y59C	TM3 π-bulge, interface with NuoK	normal	95%	57-93%	normal	(*23*, *24*)
Y59F		normal	102%	44-50%	normal	(*23*, *24*)
G61V	TM3 π-bulge, interface with NuoA	normal	99%	48-53%	normal	(*23*)
G61L		normal	98%	69-72%	normal	(*23*)
M64V	TM3 near π-bulge,	normal	96%	78-89%	60%	(*23*, *24*)
M64C		normal	105%	47%	NA	(*24*)
M64I		normal	107%	100%	normal	(*23*)
V65G	TM3 near π-bulge, interface with NuoA	normal	99%	3-13%	0%	(*23*, *24*)
V65L		normal	98%	21-23%	reduced	(*23*)
F67A	TM3	normal	86%	85%	100%	(*23*)

b) Mutations in the membrane arm, continuation

Mutation	Amino acid location	Expression/ assembly	Effect			Reference and comments
			FMN-site activity	Oxido-reductase activity	Proton pumping activity	
NuoJ						
M72V	interface with NuoA/H	NA	100%	38%	NA	(*24*)
M72A		NA	170%	126%	NA	(*24*)
M72C		NA	92%	48%	NA	(*24*)
M64V/M72A		NA	57%	53%%	NA	(*24*)
E80Q	surface, interacts with NuoK	normal	101%	100%,	normal	(*23*)
E80A		normal	102%	90%	reduced	(*23*)
Y109F	surface	NA	89%	112%	NA	(*24*)
NuoH						
E36D	Q site	normal	74%	52-77%	reduced	(*25*)
E36D		NA	91%	57%	NA	(*26*)
E36A		normal	86%	20-27	reduced	(*25*)
E36K		normal	13%	7%	BA	(*26*)
E36Q		reduced	32%	18%	NA	(*26*)
R37A	Q site, NuoB interface	no assembly	19%	1-3%	0%	(*25*)
R37K		low	36%	8-13	0%	(*25*)
Q44A	Loop1, Q site	normal	121%	45-54	NA	(*25*)
R46A	Loop1, Q site	no assembly	47%	6-13	0%	(*25*)
R46K		low	62%	23-42	reduced	(*25*)
P49A	Loop1	normal	78%	39-83	reduced	(*25*)
D63E	Q-site (entry)	normal	112%	91-93	normal	(*25*)
D63E		NA	78%	35%	NA	(*26*)
D63A		no assembly	18%	1-2%	0%	(*25*)
D63N		no assembly	24%	1%	0%	(*25*)
M64T	Q-entry	NA	86%	90%	NA	(*26*)
K70A	NuoB interface	normal	111%	93-98%	NA	(*25*)
E71A	NuoB, A interface SB to $_{A}$K46 in closed state	normal	72%	37-65%	reduced	(*25*)
G134A	near TM5-6 loop	normal	69%	70%	normal	(*25*)
G134L		no assembly	44%	7-18%	0%	(*25*)
G134V		low	54%	3-6%	0%	(*25*)
S137A	near TM5-6 loop	normal	90%	72-76%	NA	(*25*)
G145A	near TM5-6 loop	normal	114%	70-75%	normal	(*25*)
G145V		low	50%	4-5%	0%	(*25*)
R148A	NuoCD interface, SB with $_{C}$E240	low	49%	4-18	0%	(*25*)
S155A	NuoA interface	normal	95%	95-104%	NA	(*25*)
Y156A	Intramembrane surface	normal	80%	51-61%	reduced	(*25*)
E157A	E-channel, Central axis	normal	95%	24-29%	reduced	(*25*)
E157K		normal	160%	80-111%	NA	(*25*)
I201V	Intramembrane surface	NA	105%	67%	NA	(*26*)
I201T		NA	65%	59-72%	NA	(*27*)

b) Mutations in the membrane arm, continuation

Mutation	Amino acid location	Expression/ assembly	Effect			Reference and comments
			FMN-site activity	Oxido-reductase activity	Proton pumping activity	
NuoH						
V206G	Deep Intramembrane	normal	110%	95-100%	NA	(*25*)
V206E		NA	67%	63%	NA	(*28*)
R209F	Intramembrane, points into Q site	NA	59%	43%	NA	(*28*)
R209A		normal	85%	63-87%	reduced	(*25*)
H210T	Q site, NuoCD interface	NA	82%	63%	NA	(*28*)
D213A	Q site, NuoCD interface	low	53%	12%	0%	(*25*)
D213E		NA	69%	43%	NA	(*28*)
D213N		NA	95%	71%	NA	(*28*)
E216A	TM5-6 loop "beginning"	normal	112%	63-80%	NA	(*25*)
E216A		NA	95%	80%	NA	(*28*)
E218A	TM5-6 loop	normal	124%	35-43%	reduced	(*25*)
E220A	TM5-6 loop	no assembly	49%	2%	0%	(*25*)
E220Q		no assembly	45%	1%	0%	(*25*)
E228A	TM5-6 loop, NuoA, B loop interface	no assembly	40%	8%	0%	(*25*)
E228Q		no assembly	32%	1%	0%	(*25*)
E228D		NA	79%	43%	NA	(*28*)
Y229H		NA	71%	39%	NA	(*28*)
E241A	E-channel, Q site, Central axis	normal	94%	59-64%	NA	(*25*)
E241Q		normal	95%	58-60%	NA	(*25*)
R286A	Q site	normal	79%	67-63%	reduced	(*25*)
R291A	Q site	normal	126%	85-90%	NA	(*25*)
L289C	NuoI_H1 interface	NA	74%	74-81%	NA	(*29*)
R291M	near TM5-6 loop	NA	57%	57-107%	105%	(*29*)
R293M	Surface	NA	46%	46-63%	NA	(*29*)
Y294L	HB to $_{CD}$E240 from CD β-sheet	NA	89%	89-100%	NA	(*29*)
D295A	Surface, salt bridge with R291	NA	39%	39-52%	NA	(*29*)
D295A		low	58%	16-20%	0%	(*25*)
D295E		normal	98%	41-49%	reduced	(*25*)
Q296T	NuoCD interface, Interacts with lipid near $_{I}$H1	NA	63%	63-100%	NA	(*29*)
V297P	Interacts with lipid near $_{I}$H1	NA	62%	62-97%	NA	(*29*)
L289C/ V297P	near $_{I}$H1	NA	36%	36-73%	NA	(*29*)
G301C	Intramembrane surface	NA	72%	72-90%	NA	(*29*)
W302L	NuoA interface	NA	62%	62%%	100%	(*29*)
K303A	Surface/ NuoA interface	normal	71%	47-75%	reduced	(*25*)
T316H	Surface	NA	73%	72%	NA	(*27*)

References for Table S8

1. L. Euro, G. Belevich, D. A. Bloch, M. I. Verkhovsky, M. Wikström, M. Verkhovskaya, The role of the invariant glutamate 95 in the catalytic site of Complex I from Escherichia coli. *Biochim. Biophys. Acta*. **1787**, 68–73 (2009).
2. N. Castro-Guerrero, P. K. Sinha, J. Torres-Bacete, A. Matsuno-Yagi, T. Yagi, Pivotal roles of three conserved carboxyl residues of the NuoC (30k) segment in the structural integrity of proton-translocating NADH-quinone oxidoreductase from Escherichia coli. *Biochemistry*. **49**, 10072–10080 (2010).
3. P. K. Sinha, N. Castro-Guerrero, G. Patki, M. Sato, J. Torres-Bacete, S. Sinha, H. Miyoshi, A. Matsuno-Yagi, T. Yagi, Conserved amino acid residues of the NuoD segment important for structure and function of Escherichia coli NDH-1 (complex I). *Biochemistry*. **54**, 753–764 (2015).
4. G. Belevich, L. Euro, M. Wikström, M. Verkhovskaya, Role of the conserved arginine 274 and histidine 224 and 228 residues in the NuoCD subunit of complex I from Escherichia coli. *Biochemistry*. **46**, 526–533 (2007).
5. D. Flemming, P. Hellwig, S. Lepper, D. P. Kloer, T. Friedrich, Catalytic importance of acidic amino acids on subunit NuoB of the Escherichia coli NADH:ubiquinone oxidoreductase (complex I). *J. Biol. Chem.* **281**, 24781–24789 (2006).
6. D. Flemming, P. Hellwig, T. Friedrich, Involvement of tyrosines 114 and 139 of subunit NuoB in the proton pathway around cluster N2 in Escherichia coli NADH:ubiquinone oxidoreductase. *J. Biol. Chem.* **278**, 3055–3062 (2003).
7. P. K. Sinha, E. Nakamaru-Ogiso, J. Torres-Bacete, M. Sato, N. Castro-Guerrero, T. Ohnishi, A. Matsuno-Yagi, T. Yagi, Electron transfer in subunit NuoI (TYKY) of Escherichia coli NADH:quinone oxidoreductase (NDH-1). *J. Biol. Chem.* **287**, 17363–17373 (2012).
8. E. Nakamaru-Ogiso, M.-C. Kao, H. Chen, S. C. Sinha, T. Yagi, T. Ohnishi, The membrane subunit NuoL(ND5) is involved in the indirect proton pumping mechanism of Escherichia coli complex I. *J. Biol. Chem.* **285**, 39070–39078 (2010).
9. J. Michel, J. DeLeon-Rangel, S. Zhu, K. Van Ree, S. B. Vik, Mutagenesis of the L, M, and N subunits of Complex I from Escherichia coli indicates a common role in function. *PLoS One*. **6**, e17420 (2011).
10. M. Sato, P. K. Sinha, J. Torres-Bacete, A. Matsuno-Yagi, T. Yagi, Energy transducing roles of antiporter-like subunits in Escherichia coli NDH-1 with main focus on subunit NuoN (ND2). *J. Biol. Chem.* **288**, 24705–24716 (2013).
11. S. Steimle, C. Schnick, E.-M. Burger, F. Nuber, D. Krämer, H. Dawitz, S. Brander, B. Matlosz, J. Schäfer, K. Maurer, U. Glessner, T. Friedrich, Cysteine scanning reveals minor local rearrangements of the horizontal helix of respiratory complex I. *Mol. Microbiol.* **98**, 151–161 (2015).
12. G. Belevich, J. Knuuti, M. I. Verkhovsky, M. Wikström, M. Verkhovskaya, Probing the mechanistic role of the long α-helix in subunit L of respiratory Complex I from Escherichia coli by site-directed mutagenesis. *Mol. Microbiol.* **82**, 1086–1095 (2011).
13. S. Steimle, M. Willistein, P. Hegger, M. Janoschke, H. Erhardt, T. Friedrich, Asp563 of the horizontal helix of subunit NuoL is involved in proton translocation by the respiratory complex I. *FEBS Lett.* **586**, 699–704 (2012).
14. J. Torres-Bacete, E. Nakamaru-Ogiso, A. Matsuno-Yagi, T. Yagi, Characterization of the NuoM (ND4) subunit in Escherichia coli NDH-1: conserved charged residues essential for energy-coupled activities. *J. Biol. Chem.* **282**, 36914–36922 (2007).
15. J. Torres-Bacete, P. K. Sinha, N. Castro-Guerrero, A. Matsuno-Yagi, T. Yagi, Features of subunit NuoM (ND4) in Escherichia coli NDH-1: TOPOLOGY AND IMPLICATION OF CONSERVED GLU144 FOR COUPLING SITE 1. *J. Biol. Chem.* **284**, 33062–33069 (2009).
16. L. Euro, G. Belevich, M. I. Verkhovsky, M. Wikström, M. Verkhovskaya, Conserved

lysine residues of the membrane subunit NuoM are involved in energy conversion by the proton-pumping NADH:ubiquinone oxidoreductase (Complex I). *Biochim. Biophys. Acta*. **1777**, 1166–1172 (2008).
17. M. E. Mühlbauer, P. Saura, F. Nuber, A. Di Luca, T. Friedrich, V. R. I. Kaila, Water-Gated Proton Transfer Dynamics in Respiratory Complex I. *J. Am. Chem. Soc.* **142**, 13718–13728 (2020).
18. B. Amarneh, S. B. Vik, Mutagenesis of subunit N of the Escherichia coli complex I. Identification of the initiation codon and the sensitivity of mutants to decylubiquinone. *Biochemistry*. **42**, 4800–4808 (2003).
19. M.-C. Kao, E. Nakamaru-Ogiso, A. Matsuno-Yagi, T. Yagi, Characterization of the membrane domain subunit NuoK (ND4L) of the NADH-quinone oxidoreductase from Escherichia coli. *Biochemistry*. **44**, 9545–9554 (2005).
20. J. Torres-Bacete, P. K. Sinha, M. Sato, G. Patki, M.-C. Kao, A. Matsuno-Yagi, T. Yagi, Roles of subunit NuoK (ND4L) in the energy-transducing mechanism of Escherichia coli NDH-1 (NADH:quinone oxidoreductase). *J. Biol. Chem.* **287**, 42763–42772 (2012).
21. M. Kervinen, J. Pätsi, M. Finel, I. E. Hassinen, A pair of membrane-embedded acidic residues in the NuoK subunit of Escherichia coli NDH-1, a counterpart of the ND4L subunit of the mitochondrial complex I, are required for high ubiquinone reductase activity. *Biochemistry*. **43**, 773–781 (2004).
22. M.-C. Kao, S. Di Bernardo, M. Perego, E. Nakamaru-Ogiso, A. Matsuno-Yagi, T. Yagi, Functional roles of four conserved charged residues in the membrane domain subunit NuoA of the proton-translocating NADH-quinone oxidoreductase from Escherichia coli. *J. Biol. Chem.* **279**, 32360–32366 (2004).
23. M.-C. Kao, S. Di Bernardo, E. Nakamaru-Ogiso, H. Miyoshi, A. Matsuno-Yagi, T. Yagi, Characterization of the membrane domain subunit NuoJ (ND6) of the NADH-quinone oxidoreductase from Escherichia coli by chromosomal DNA manipulation. *Biochemistry*. **44**, 3562–3571 (2005).
24. J. Pätsi, M. Kervinen, M. Finel, I. E. Hassinen, Leber hereditary optic neuropathy mutations in the ND6 subunit of mitochondrial complex I affect ubiquinone reduction kinetics in a bacterial model of the enzyme. *Biochem. J.* **409**, 129–137 (2008).
25. P. K. Sinha, J. Torres-Bacete, E. Nakamaru-Ogiso, N. Castro-Guerrero, A. Matsuno-Yagi, T. Yagi, Critical roles of subunit NuoH (ND1) in the assembly of peripheral subunits with the membrane domain of Escherichia coli NDH-1. *J. Biol. Chem.* **284**, 9814–9823 (2009).
26. J. Pätsi, P. Maliniemi, S. Pakanen, R. Hinttala, J. Uusimaa, K. Majamaa, T. Nyström, M. Kervinen, I. E. Hassinen, LHON/MELAS overlap mutation in ND1 subunit of mitochondrial complex I affects ubiquinone binding as revealed by modeling in Escherichia coli NDH-1. *Biochim. Biophys. Acta*. **1817**, 312–318 (2012).
27. R. Hinttala, M. Kervinen, J. Uusimaa, P. Maliniemi, S. Finnilä, H. Rantala, A. M. Remes, I. E. Hassinen, K. Majamaa, Analysis of functional consequences of haplogroup J polymorphisms m.4216T>C and m.3866T>C in human MT-ND1: mutagenesis of homologous positions in Escherichia coli. *Mitochondrion*. **10**, 358–361 (2010).
28. M. Kervinen, R. Hinttala, H. M. Helander, S. Kurki, J. Uusimaa, M. Finel, K. Majamaa, I. E. Hassinen, The MELAS mutations 3946 and 3949 perturb the critical structure in a conserved loop of the ND1 subunit of mitochondrial complex I. *Hum. Mol. Genet.* **15**, 2543–2552 (2006).
29. P. Maliniemi, M. Kervinen, I. E. Hassinen, Modeling of human pathogenic mutations in Escherichia coli complex I reveals a sensitive region in the fourth inside loop of NuoH. *Mitochondrion*. **9**, 394–401 (2009).